

# PtuA and PtuB assemble into an inflammasome-like oligomer for anti-phage defense

Received: 22 February 2023

Accepted: 3 November 2023

Published online: 4 January 2024

 Check for updates

Yuanyuan Li<sup>1,6</sup>, Zhangfei Shen<sup>2,3,6</sup>, Mengyuan Zhang<sup>1,6</sup>, Xiao-Yuan Yang<sup>2,3,4,6</sup>, Sean P. Cleary<sup>5</sup>, Jiale Xie<sup>2,3,4</sup>, Ila A. Marathe<sup>5</sup>, Marius Kostelic<sup>5</sup>, Jacelyn Greenwald<sup>5</sup>, Anthony D. Rish<sup>2,3,4</sup>, Vicki H. Wysocki<sup>5</sup>, Chong Chen<sup>1</sup>, Qiang Chen<sup>1</sup>✉, Tian-Min Fu<sup>2,3,4</sup>✉ & Yamei Yu<sup>1</sup>✉

*Escherichia coli* Septu system, an anti-phage defense system, comprises two components: PtuA and PtuB. PtuA contains an ATPase domain, while PtuB is predicted to function as a nuclease. Here we show that PtuA and PtuB form a stable complex with a 6:2 stoichiometry. Cryo-electron microscopy structure of PtuAB reveals a distinctive horseshoe-like configuration. PtuA adopts a hexameric arrangement, organized as an asymmetric trimer of dimers, contrasting the ring-like structure by other ATPases. Notably, the three pairs of PtuA dimers assume distinct conformations and fulfill unique roles in recruiting PtuB. Our functional assays have further illuminated the importance of the oligomeric assembly of PtuAB in anti-phage defense. Moreover, we have uncovered that ATP molecules can directly bind to PtuA and inhibit the activities of PtuAB. Together, the assembly and function of the Septu system shed light on understanding other ATPase-containing systems in bacterial immunity.

The perpetual arms race between bacteria and bacteriophages has spurred bacteria to evolve intricate immune networks as a defense against phage attacks. Over the past few decades, a multitude of bacterial immune systems have been discovered and characterized<sup>1–3</sup>, including restriction–modification systems<sup>4</sup>, CRISPR–Cas systems<sup>5,6</sup>, prokaryotic Argonautes systems<sup>7,8</sup> and cyclic oligonucleotide-based anti-phage signaling systems<sup>9</sup>. Investigating these bacterial immune systems has transformed biomedical research. One illustration of this transformative impact can be seen in the study of CRISPR–Cas systems, which has revolutionized genome editing<sup>10–12</sup>. Moreover, mechanistic understanding of these bacterial immune systems has yielded unprecedented insights into the origin and evolution of mammalian immune systems. Many immune mechanisms, initially believed to be

evolutionary novelties exclusive to metazoans, have been discovered in bacteria. This suggests that key components of immune systems in higher organisms may have their origins in bacterial homologs. For example, the cyclic GMP–AMP synthase (cGAS)–stimulator of interferon genes (STING) pathway, a major innate immune defense mechanism in higher organisms, couples double-strand DNA sensing with the induction of immune response<sup>13,14</sup>. Recent studies revealed that bacteria cyclic oligonucleotide-based anti-phage signaling systems also encode cGAS-like proteins capable of activating downstream STING-like effector proteins, thereby serving as a parallel of cGAS–STING axis in the realm of anti-phage immune defense<sup>15–17</sup>.

By mining the microbe pangenome, many bacterial immune systems with diverse compositions have been discovered, including Thois, and

<sup>1</sup>Department of Biotherapy, Cancer Center and State Key Laboratory of Biotherapy, West China Hospital, Sichuan University, Chengdu, P. R. China.

<sup>2</sup>Department of Biological Chemistry and Pharmacology, The Ohio State University, Columbus, OH, USA. <sup>3</sup>The Ohio State University Comprehensive Cancer Center, Columbus, OH, USA. <sup>4</sup>The Ohio State Biochemistry Program, The Ohio State University, Columbus, OH, USA. <sup>5</sup>Department of Chemistry and Biochemistry, The Ohio State University, Columbus, OH, USA. <sup>6</sup>These authors contributed equally: Yuanyuan Li, Zhangfei Shen, Mengyuan Zhang, Xiao-Yuan Yang. ✉e-mail: [qiang\\_chen@scu.edu.cn](mailto:qiang_chen@scu.edu.cn); [fu.978@osu.edu](mailto:fu.978@osu.edu); [yamei\\_yu@scu.edu.cn](mailto:yamei_yu@scu.edu.cn)

Hachiman, Shedu, Gabija, Septu, Lamassu, Zorya, Kiwa, Druantia, Wadjet and AVAST systems<sup>18,19</sup>. However, the mechanisms by which these systems restrict the infection and amplification of phages remain largely unexplored. Some of these newly identified systems, including the Septu, Gabijia and Lamassu systems, contain components with ATPase domains and nuclease domains, suggesting that these systems may use a similar mechanism to battle bacteriophage infection. The Septu system has two components: PtuA and PtuB. Sequence analysis reveals that PtuA contains an ATPase domain while PtuB is a nuclease that belongs to the His–Asn–His (HNH) family<sup>20,21</sup>. As PtuB is a nuclease, it is highly possible that the Septu system utilized PtuB to cleave the genomic DNA of invading bacteriophages. Despite this limited understanding, the assembly and function of PtuAB in anti-phage defense remain unclear.

In this Article, our structural and functional analysis revealed intriguing mechanisms of the Septu system in anti-phage defense. Our biochemical reconstitution and native mass spectrometry analysis demonstrate that PtuA and PtuB assemble into a stable complex with a stoichiometry of 6:2. Further cryo-electron microscopy (cryo-EM) structural analysis reveals that PtuA assembles into a hexamer by forming an asymmetric trimer of dimers. The three pairs of PtuA dimers display different conformations, with two pairs of PtuA dimers favorably interacting with PtuB, explaining the 6:2 stoichiometry of PtuA and PtuB in the complex. Biochemical and cellular assays show that PtuAB restricts phage growth by cleaving phage genomic DNA. Finally, ATP molecules can bind to PtuA and modulate the PtuAB nuclease activity. Together, we show that PtuA and PtuB can assemble into an inflammasome-like complex for anti-phage defense, a mechanism that may be universally shared by many other newly identified bacteria immune systems.

## Results

### PtuA and PtuB form an oligomeric complex

To gain a comprehensive understanding of the Septu system across species, we identified Septu systems from more than 400 bacteria species and performed a deep sequence analysis. Despite the sequence diversity of the Septu systems, all the PtuA from different species are composed of an N-terminal ATPase domain followed by a C-terminal triple-helix domain (CTD), while PtuB is a nuclease (Fig. 1a and Extended Data Figs. 1 and 2a,b).

To biochemically characterize the Septu system, we reconstituted the *Escherichia coli* Septu system by purifying PtuA and PtuB overexpressed in *E. coli* BL21(DE3). We found that PtuA alone can be overexpressed and purified as soluble forms in *E. coli* (Extended Data Fig. 2c). In contrast, PtuB alone was expressed as inclusion bodies in *E. coli* (Extended Data Fig. 2d), suggesting that PtuB failed to fold well when expressed alone in *E. coli*. To test whether PtuA and PtuB can form a stable complex, we co-expressed PtuA and PtuB in *E. coli* with PtuB containing a C-terminal His<sub>6</sub> tag. The co-migration of PtuA and PtuB on gel filtration suggested that they assembled into a stable complex (Fig. 1b,c). Unexpectedly, over-stoichiometry of PtuA to PtuB was observed in the reconstituted PtuAB complex (Fig. 1c). To further determine the stoichiometry of PtuA and PtuB, we performed native mass spectrometry analysis of the purified complexes and found that PtuA and PtuB form a heteromeric complex with a 6:2 stoichiometry (Fig. 1d).

### Overall structure of PtuA hexamer

To understand the assembly of PtuA, we determined the cryo-EM structure of PtuA with a resolution of 2.9 Å (Fig. 2a, Table 1 and Extended Data Figs. 3 and 4a), which enabled us to build an atomic model de novo. After we built up the structural model, we were surprised to find that the horseshoe-like structure is composed of six copies of the PtuA ATPase domain (Fig. 2b). The six molecules of the PtuA ATPase domain assemble as an asymmetric trimer of dimers to form the hexamer with dimensions of 115 Å × 110 Å × 70 Å (Fig. 2a,b).

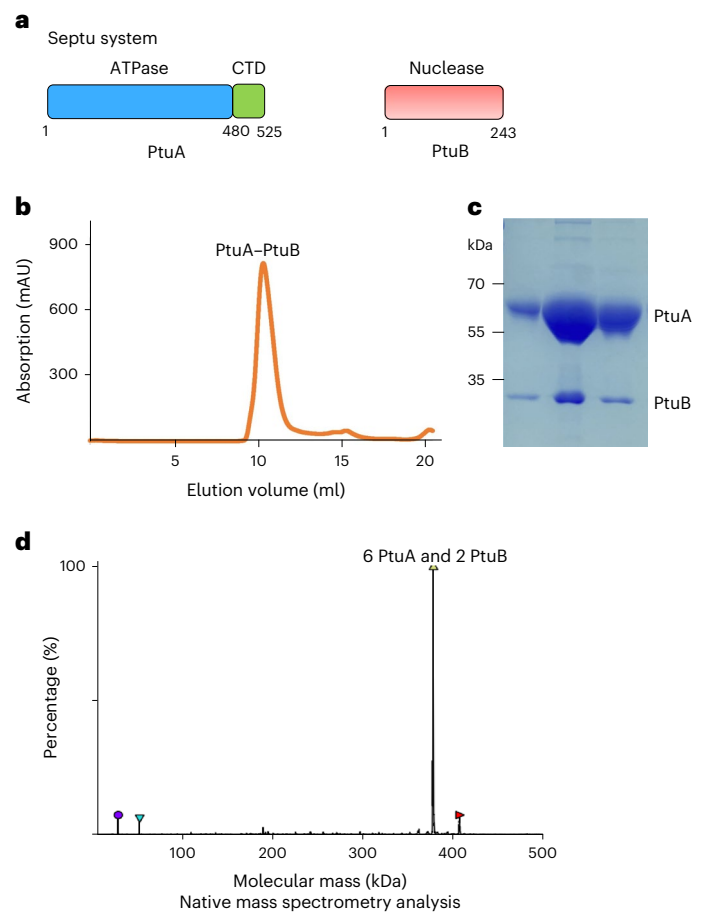


**Fig. 1 | Reconstitution of the PtuA and PtuB complex.** **a**, Domain organization of PtuA and PtuB with residue numbers indicated below. **b**, Gel filtration profile of the PtuA and PtuB complex that are co-expressed and purified. **c**, SDS–PAGE analysis showing the purified PtuA and PtuB complex. The experiment was replicated at least three times. **d**, Native mass spectrometry analysis of the PtuA and PtuB complex, revealing a 6:2 stoichiometry of PtuA and PtuB.

The PtuA ATPase domain folds into an ellipsoidal architecture with convex and concave sides, which can be divided into two lobes (Fig. 2c). The N-terminal lobe (N-lobe) assembles as an  $\alpha/\beta$  roll via the packing of  $\alpha$ A against an antiparallel  $\beta$ -sheet with 7  $\beta$  strands in the order of 8, 7, 6, 1, 2, 16 and 15. In contrast, the C-terminal lobe (C-lobe) adopts a  $\beta$ - $\alpha$ - $\beta$  fold containing a central  $\alpha$ -helical bundle of  $\alpha$ D,  $\alpha$ E and  $\alpha$ F that is sandwiched by a five-stranded mixed  $\beta$  sheet ( $\beta$ -sheet II containing strands 9, 13, 14 and 3) and a three-stranded antiparallel  $\beta$  sheet ( $\beta$ -sheet III containing strands 10, 11 and 12). The two lobes are connected via a long  $\alpha$ -helix of  $\alpha$ B. DALI search showed that the PtuA ATPase domain resembles the ATPase domain of Rad50 (ref. 22). Overlaid structures of PtuA and Rad50 revealed some features unique to PtuA. First, compared to Rad50, PtuA has an inserted  $\beta$ -hairpin formed by  $\beta$ 5 and  $\beta$ 6 in its N-lobe (Fig. 2d), which is important for the hexamer assembly of PtuA (see next section). Second,  $\alpha$ C and  $\alpha$ D of PtuA form an  $\alpha$ -hairpin in the C-lobe (Fig. 2d), which is also involved in the oligomerization of PtuA (see next section).

### Assembly of PtuA hexamer

The hexamer of PtuA is organized by three pairs of PtuA dimers, in which two pairs of PtuA dimers, hereafter referred to as side dimers, resemble each other and are different from the third pair, denoted as a central dimer (Fig. 2b). The differences between PtuA side dimer and central dimer lie in two aspects. First, the central dimer contains two ATP molecules in the dimeric interface, while each side dimer coordinates one

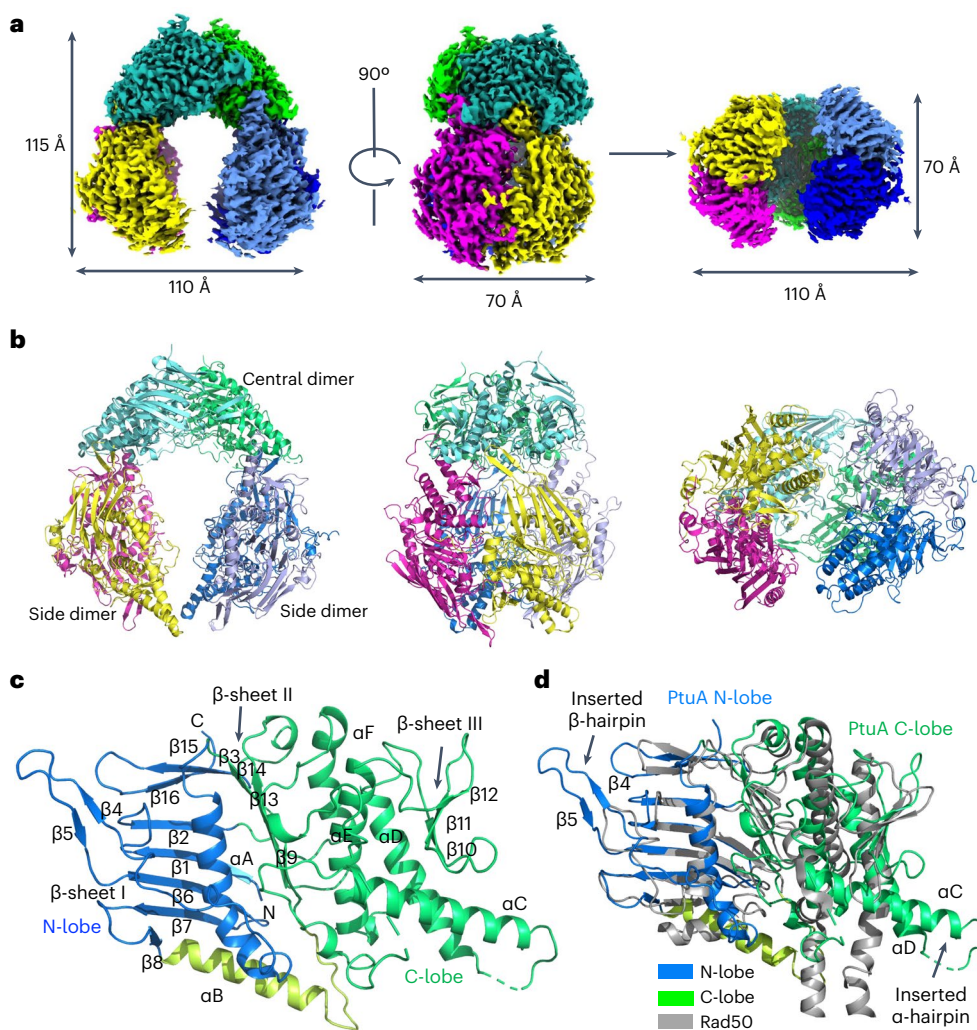


**Fig. 2 | Overall structure of PtuA hexamer. a**, The cryo-EM density map of PtuA hexamer with each subunit colored individually. The hexamer has estimated dimensions of 115 Å by 110 Å by 70 Å. **b**, Ribbon diagrams of PtuA hexamer with subunits colored in green, cyan, yellow, magenta, blue and light blue. **c**, Ribbon

diagram of PtuA N-terminal domain (NTD) with secondary structures labeled. The N-lobe and C-lobe of PtuA NTD are colored in blue and green, respectively. **d**, Overlaid structures of PtuA NTD (green and blue) and Rad50 (gray), revealing the  $\beta$ -hairpin and  $\alpha$ -hairpin unique to PtuA.

ATP molecule (Fig. 3a,b). Second, overlaid structures of the side dimer and central dimer revealed dramatic conformational changes in the  $\beta$ -hairpin and  $\alpha$ -hairpin regions (Fig. 3c). Despite the differences above, both the central dimer and the side dimers are formed by two protomers of PtuA in a head-to-tail manner, in which each N-lobe mutually engages with the C-lobe of the opposing PtuA protomer, resembling the dimeric arrangement of Rad50 (Fig. 3a–c and Extended Data Fig. 4b). The dimeric interface displays a long groove, 75 Å in length, that runs through the PtuA dimer. Moreover, both the central dimer and the side dimer have a buried interface area of more than 3,000 Å<sup>2</sup>. In both the central dimer and the side dimers, the dimeric interfaces are mediated by  $\beta$ -hairpin,  $\beta$ -sheet III and many loops from each protomer. Hydrophobic and hydrophilic residues establish an extensive interaction network in the dimeric interfaces for both the central dimer and the side dimers (Extended Data Fig. 4c).

Interactions between PtuA central dimer and the two side dimers establish the structural basis of the PtuA hexamer assembly. The central dimer is located in the middle for the engagement of two pairs of side dimers using the dimer–dimer interface, which is mediated by the  $\beta$ -hairpin in the N-lobe and  $\alpha$ -hairpin in the C-lobe of PtuA ATPase domain (Fig. 3d). Residues R73, Q78, E79, E84 in the  $\beta$ -hairpin from one subunit of the side dimer establish hydrophilic interactions with

residues E138, E224, R227 and R179, respectively, in the  $\alpha$ -hairpin of one subunit in the central dimer. Residues L81 and Y76 in the  $\beta$ -hairpin of the side dimer pack against residues W202, R230 and R227 in the  $\alpha$ -hairpin of the central dimer through hydrophobic interactions (Fig. 3e). Meanwhile, residues from the  $\alpha$ -hairpin of the other subunit in the side dimer also establish interacting networks with residues from the  $\alpha$ -hairpin of a subunit in the central dimer (Fig. 3f). Together, these interaction networks constitute the foundation of PtuA oligomerization.

To validate the functional importance of residues on the PtuA dimer–dimer interface, we mutated L81 into arginine and tested the oligomerization of the PtuA L81R mutant. Mass photometry analysis revealed that L81R mutant predominantly exists as a dimer with a small population of monomers, consistent with our gel filtration analysis (Fig. 3g and Extended Data Fig. 4d). We further co-expressed PtuA L81R mutant with PtuB to test whether the mutant PtuA can assemble into a complex with PtuB. After purification, we found that the PtuA L81R mutant failed to form a stable complex with PtuB (Fig. 3h), suggesting that the hexameric assembly of PtuA is critical for the recruitment of PtuB.

#### ATP binding sites

Structural analysis revealed four ATP molecules in the hexameric PtuA. ATP molecules are buried in the PtuA dimeric interface, sandwiched

**Table 1 | Cryo-EM data collection, refinement and validation statistics**

	PtuA_Hexamer(from PtuAB dataset) (EMDB-28045),(PDB 8EE4)	PtuAB Focused (EMDB-28048),(PDB 8EE7)	PtuAB Composite (EMDB-28049),(PDB 8EEA)	PtuA_Hexamer(apo state) (EMDB-40779),(PDB 8SUX)
<b>Data collection and processing</b>				
Magnification	81,000	81,000	81,000	81,000
Voltage (kV)	300	300	300	300
Electron exposure ( $e^- \text{Å}^{-2}$ )	50	50	50	50
Defocus range ( $\mu\text{m}$ )	0.5–2.5	0.5–2.5	0.5–2.5	0.5–2.5
Pixel size ( $\text{Å}$ )	1.12	1.12	1.12	1.12
Symmetry imposed	C2	C1	n/a	C2
Initial images (no.)	7,042	7,042	7,042	6,992
Initial particle images (no.)	11,830,802	11,830,802	11,830,802	11,005,697
Final particle images (no.)	2,307,662	1,832,915	n/a	779,494
Map resolution ( $\text{Å}$ )	2.60	2.72	n/a	2.93
Fourier shell correlation (FSC) threshold	0.143	0.143		0.143
Map resolution range ( $\text{Å}$ )	2.50–3.20	2.60–3.20	2.50–3.20	2.50–4.00
<b>Refinement</b>				
Initial model used (PDB code)	AlphaFold	AlphaFold	AlphaFold	AlphaFold
Model resolution ( $\text{Å}$ )	3.0	3.0	2.7	3.0
FSC threshold	0.5	0.5	0.5	0.5
Model resolution range ( $\text{Å}$ )	2.6–3.5	2.7–3.6	2.7–4.5	3.0–5.0
Map sharpening $B$ factor ( $\text{Å}^2$ )	–123.3	–115.3	n/a	–138.0
<b>Model composition</b>				
Non-hydrogen atoms	18881	9188	24480	18101
Protein residues	2310	1135	3017	2231
Ligands (ATP)	4	1	4	4
<b><math>B</math> factors (<math>\text{Å}^2</math>)</b>				
Protein	33.01	40.57	60.66	71.20
Ligand	34.48	28.95	48.73	65.42
<b>Root mean square deviations</b>				
Bond lengths ( $\text{Å}$ )	0.002	0.003	0.004	0.003
Bond angles ( $^\circ$ )	0.629	0.517	0.953	0.533
<b>Validation</b>				
MolProbity score	1.48	1.20	1.21	1.44
Clashscore	3.98	1.75	1.97	3.82
Poor rotamers (%)	0.00	0.00	0.00	0.00
<b>Ramachandran plot</b>				
Favored (%)	95.71	96.07	96.31	96.05
Allowed (%)	4.29	3.93	3.69	3.95
Disallowed (%)	0.00	0.00	0.00	0.00

between the Walker A and B motifs of one protomer and the conserved signature motif from the other protomer in PtuA dimer (Fig. 4a,b and Extended Data Fig. 1). Residues R12, Y272 and Q279 are responsible for coordinating the adenyl group and sugar ring of ATP while K36, D282 and N160 interact with the phosphate groups (Fig. 4b). Electrostatic surface analysis showed that ATP was nested in a shallow pocket of PtuA with the adenyl group in a hydrophobic environment and the phosphate groups surrounded by positively charged residues (Fig. 4c). There are two ATP molecules in the central dimer while one ATP molecule binds to each pair of the side dimers (Fig. 3a,b). In comparison to the central dimer, a larger cleft at one side of the side dimer led to key residues

for ATP coordination rotating away from the ATP molecule in the side dimers (Extended Data Fig. 5a,b). As such, this site in the side dimer is unfavorable for coordinating ATP.

As ATP molecules were observed in PtuA, we hypothesized that PtuA may not be capable of hydrolyzing ATP. We performed an ATPase activity assay using a phosphate detection kit to test this hypothesis. Compared to the positive control, no ATPase activity was detected in either PtuA or PtuAB, providing evidence that neither PtuA alone nor PtuAB complex can hydrolyze ATP (Fig. 4d). A previous study revealed that key residues and  $\text{Mg}^{2+}$  in the active site of Rad50 formed a hydrogen bond network poised for ATP hydrolysis<sup>23</sup> (Extended Data Fig. 6a).

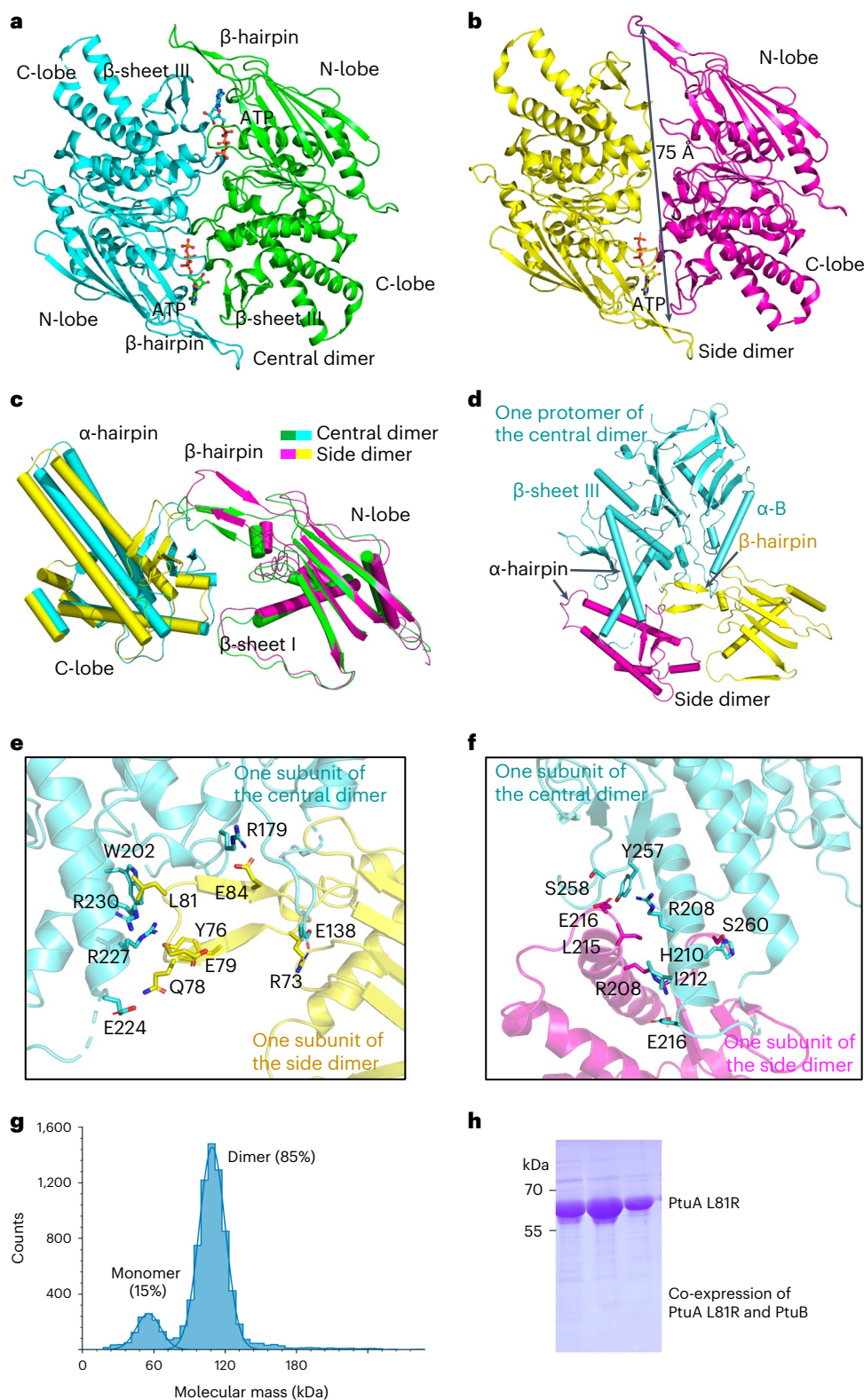


**Fig. 3 | The Assembly of PtuA hexamer.** **a**, Ribbon diagram of the PtuA central dimer with two ATP molecules. Key elements mediating PtuA dimerization were labeled. **b**, Ribbon diagram of the PtuA side dimer with one ATP molecule. The dimeric interface of PtuA is about 75 Å in length. **c**, Overlaid structures of the PtuA central dimer (green and cyan) and the PtuA side dimer (yellow and magenta). **d**, Interfaces of PtuA central dimer and PtuA side dimer mediated by  $\alpha$ -hairpins and  $\beta$ -hairpin. **e**, Residues mediating the interactions of  $\alpha$ -hairpin from one

PtuA subunit in the central dimer (cyan) and  $\beta$ -hairpin from one PtuA subunit in one side dimer (yellow). **f**, Residues mediating the interactions of  $\alpha$ -hairpin from one PtuA subunit in the central dimer (cyan) and  $\alpha$ -hairpin from one PtuA subunit in one side dimer (magenta). **g**, Mass spectrometry analysis revealed the oligomerization status of PtuA L81R. **h**, SDS-PAGE analysis showing the purified PtuA L81R co-expressed with PtuB, revealing that PtuA L81R failed to recruit PtuB. The experiment was replicated three times.

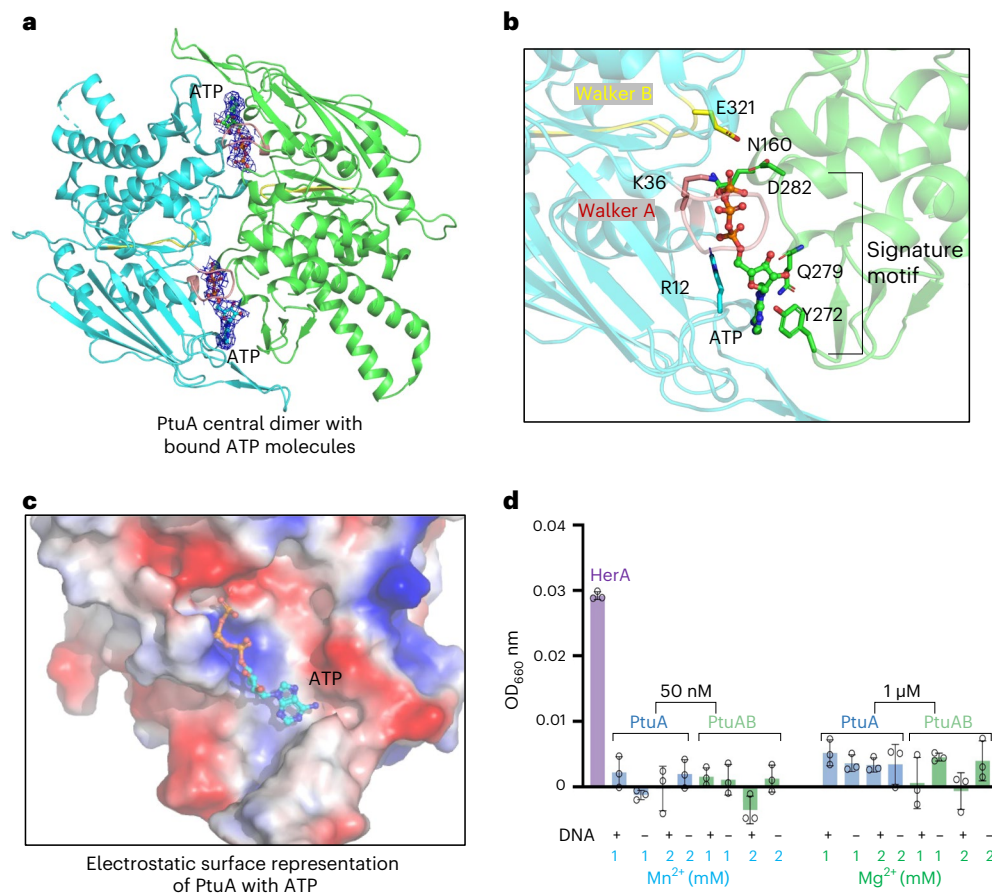


**Fig. 4 | ATP binding sites in PtuA.** **a**, Two ATP molecules bind to PtuA central dimer with the cryo-EM density maps ( $2.0\sigma$ ). **b**, Residues of PtuA coordinating ATP molecule highlighted in sticks. The highly conserved Walker A motif and Walker B motif were highlighted in red and in yellow, respectively. The signature motif critical for coordinating ATP spanning from Y272 to D282 was highlighted

by a square bracket. **c**, Electrostatic surface representation of one PtuA subunit showing the binding pocket of ATP. **d**, ATP hydrolysis assay revealing that neither PtuA alone nor PtuAB complex has ATPase activity. *E. coli* HerA, an ATPase, serves as a positive control. Histograms correspond to the mean of three independent experiments; error bars represent the s.d.

In contrast, the unique configurations of ATP in PtuA and the substitution of a key Gln residue with Gly in PtuA probably lead to the deficiency of ATP hydrolysis by PtuA (Extended Data Fig. 6b–d).

### Cryo-EM structure of the PtuAB complex

To understand the assembly of the PtuAB complex, we collected cryo-EM images of the PtuAB complex for structure determination (Extended Data Fig. 7a). During our initial structural reconstruction, we picked particles using a box size of 216 pixels (about 242 Å) (Extended Data Fig. 7b). After multiple rounds of 2D and 3D classification, we obtained a cryo-EM map in which only PtuA is visible (Extended Data Fig. 7b–d). To obtain the cryo-EM structure of PtuAB, we reprocessed our cryo-EM data by re-picking particles using a larger box size of 256 pixels (about 287 Å) (Extended Data Fig. 8a). We first obtained a cryo-EM map of 5 Å, which reveals two additional densities that are tightly associated with PtuA side dimers in comparison to the PtuA hexamer map (Extended Data Fig. 8b). We further generated a mask to perform focused refinement on one side dimer with the newly identified blob, resulting in a high-resolution map of 2.7 Å for model building (Fig. 5a, Table 1 and Extended Data Fig. 8a,c). Based on these cryo-EM maps, we obtained a high-resolution composite map of the PtuAB complex to build a structural model in which there are two PtuB molecules and six PtuA molecules (Fig. 5b,c). Each side dimer of PtuA interacts with one PtuB molecule while the central dimer does not recruit any PtuB molecule, suggesting a functional difference between the central dimer and side dimers (Fig. 5c). Furthermore, the CTDs of PtuA in the

side dimers, which are responsible for the recruitment of PtuB, were clearly resolved in the PtuAB complex. In contrast, the CTD of PtuA in the central dimer remains absent. These observations suggest that the interaction between PtuB and PtuA CTD may stabilize the conformation of PtuA CTD. Detailed structural analysis showed that PtuB sits in a cleft formed by the two CTDs of PtuA side dimers and establishes extensive interactions with the two protomers of each PtuA side dimer in an asymmetric way (Fig. 5c–i). PtuB folds as an  $\alpha/\beta$  roll with five  $\alpha$ -helices and three  $\beta$ -strands (Fig. 5f). The long  $\alpha$ -5 helix in PtuB is sandwiched by  $\alpha$ -helices of the PtuA CTD (Fig. 5g). PtuB establishes extensive interactions with helices  $\alpha$ -G and  $\alpha$ -J in one PtuA CTD, whereas PtuB  $\alpha$ -5 forms a few interactions with the  $\alpha$ -J helix of the other PtuA subunit in the side dimer (Fig. 5h,i). Notably, many hydrophobic residues in PtuB are buried by the CTD of PtuA (Fig. 5h,i), explaining why PtuB alone cannot be expressed as a soluble form in *E. coli*.

### Catalytic mechanism of the PtuAB complex

DALI search showed that PtuB belongs to the HNH nuclease superfamily with a catalytic core resembling that of Cas9 NHN domain<sup>22,24</sup> (Extended Data Fig. 9a). Residues D839, H840, N854 and N863 were shown to be critical for the catalysis of Cas9 (ref. 24) (Extended Data Fig. 9b). An alignment between the catalytic cores of PtuB and Cas9 identified residues E71, H72, N88 and H114 in PtuB that are in positions equivalent to that of the catalytic residues in Cas9 (Fig. 6a and Extended Data Fig. 9b). To test the functional importance of these residues in catalysis, we developed a plasmid nicking assay (Fig. 6b). In comparison to the

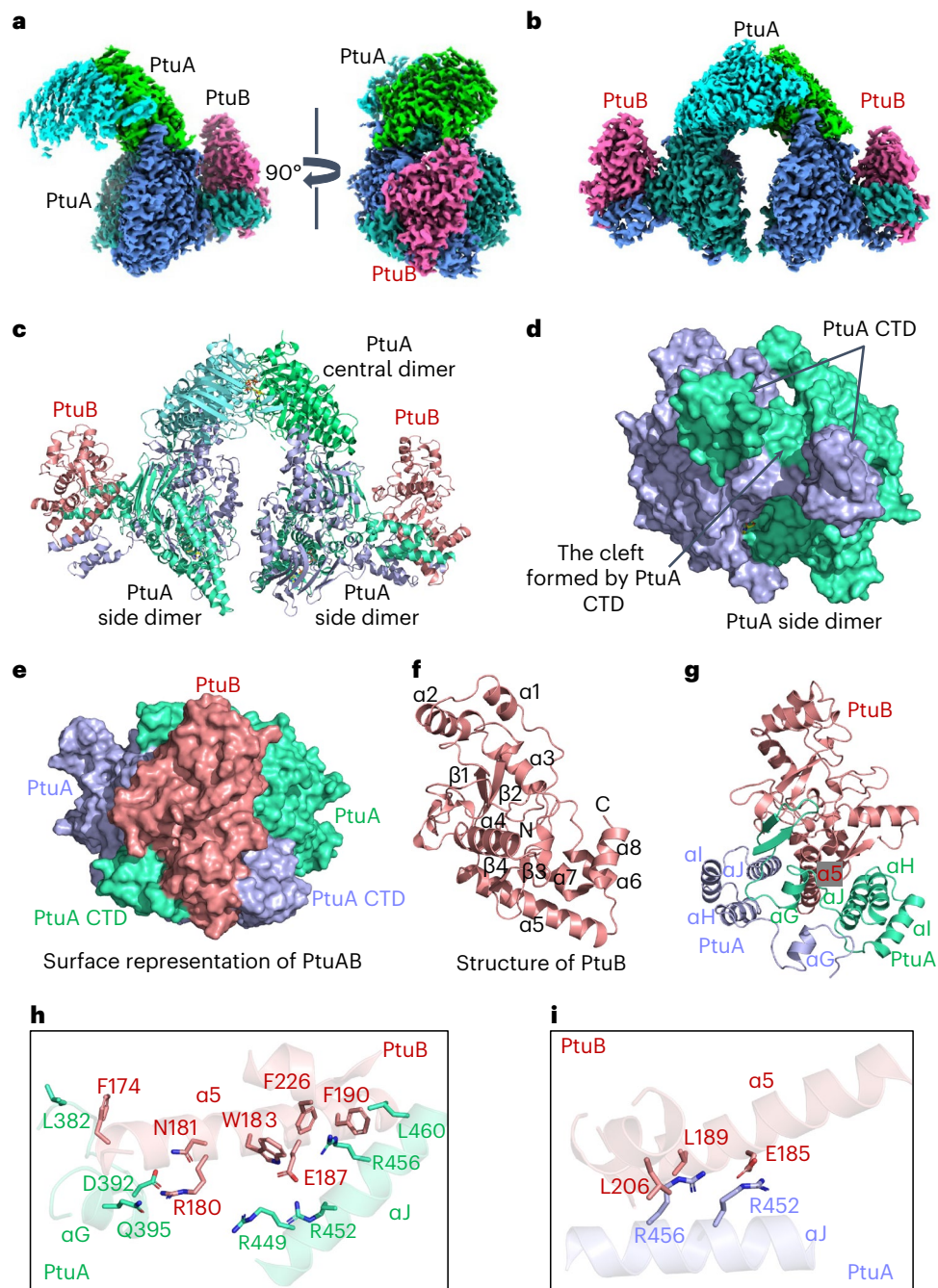


**Fig. 5 | The assembly of the PtuA and PtuB complex.** **a**, The focus-refined cryo-EM density map of the PtuA and PtuB complex with each subunit colored individually. **b**, The composite cryo-EM density map of the PtuA (green, cyan and blue) and PtuB (red) complex. **c**, Ribbon diagram of the PtuA and PtuB complex with subunits color coded. **d**, Surface representation of a PtuA side dimer, showing the cleft formed by PtuA CTD. **e**, Surface representation of a PtuA side

dimer in complex with PtuB (Red), revealing that PtuB was sandwiched by the CTD of PtuA. **f**, Ribbon diagram of PtuB with all the secondary structures labeled. **g**, Ribbon diagram of PtuB and PtuA CTD, revealing that the  $\alpha$ -5 helix of PtuB is surrounded by the  $\alpha$ -helices of PtuA CTD. **h**, Detailed interactions between PtuB and one subunit of PtuA side dimer. **i**, Residues on the interface of PtuB and the other subunit of PtuA side dimer.

wild type, alanine substitutions of residues H72 and N88 in PtuB led to the loss of catalytic activity, suggesting that PtuB degrades DNA in a similar way as HNH endonucleases (Fig. 6c). In addition, compared to the active site of Cas9 NHN domain, key residues in the active site of PtuB are not perfectly aligned for catalysis and conformational reorganization of the active site may be required for the activation of PtuB (Extended Data Fig. 9b). Together, we propose that PtuB may adopt a similar catalytic mechanism with Cas9, in which H72 serves as a general base to activate a water molecule for the attack of a phosphodiester

bond while the other three residues in the catalytic center may coordinate a divalent cation to stabilize the conformation of nucleotides (Extended Data Fig. 9b).

To test the roles of divalent cations in PtuB catalysis, we performed the plasmid nicking assay in the presence of different divalent cations at different concentrations. We found that both  $Mn^{2+}$  and  $Mg^{2+}$  can substantially promote the activity of PtuAB in a concentration-dependent manner (Fig. 6d). In contrast,  $Zn^{2+}$  did not potentiate the nuclease activity of PtuAB (Fig. 6d). Considering that  $Mg^{2+}$  is the most abundant

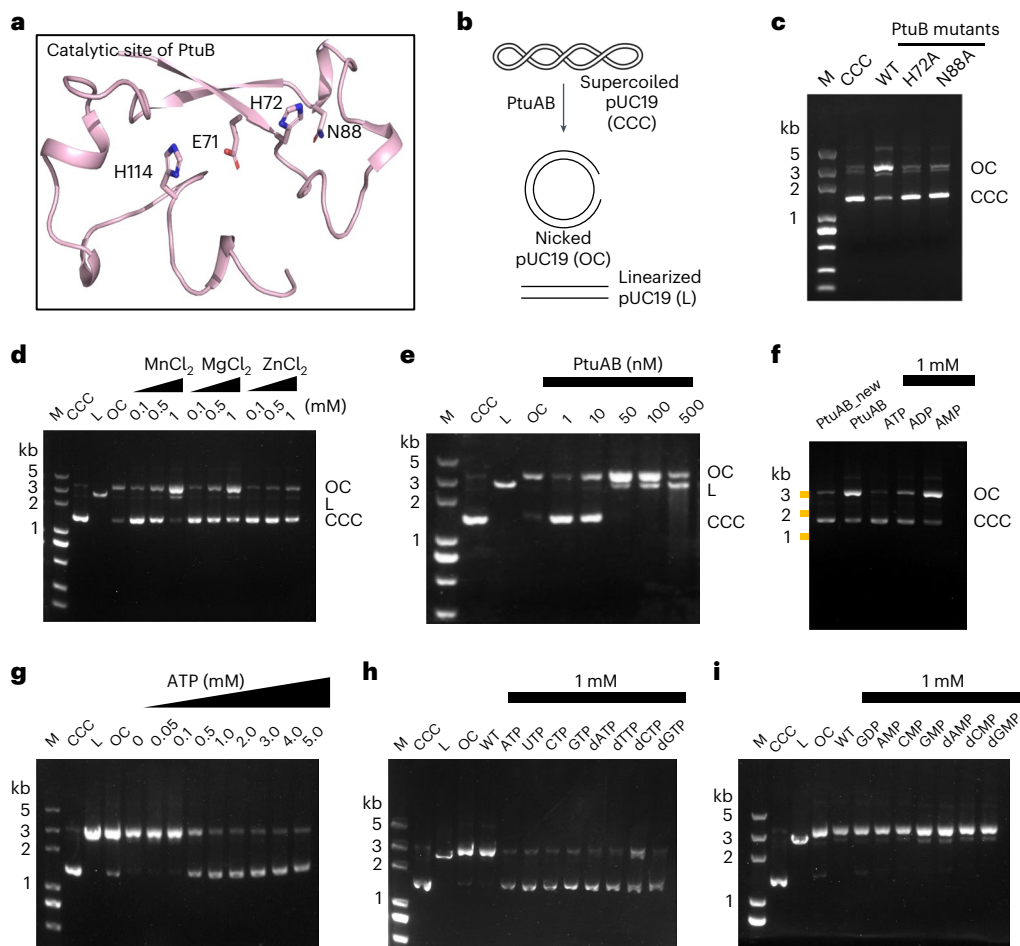


**Fig. 6 | Catalytic mechanisms of the PtuA and PtuB complex.** **a**, The catalytic site of PtuB with potential catalytic residues highlighted as sticks. **b**, Diagram illustrating the plasmid nicking assay by the PtuA and PtuB complex. **c**, Plasmid nicking activities of PtuB wild type and mutants. All the assays were replicated at least three times. **d**, Effects of  $Mn^{2+}$ ,  $Mg^{2+}$  and  $Zn^{2+}$  on the catalysis of the PtuA and PtuB complex. All the assays were replicated at least three times. **e**, The PtuA and PtuB complex processes plasmids in a concentration-dependent manner. All the assays were replicated at least three times. **f**, Effects of ATP, AMP and ADP on the

catalysis of the PtuA and PtuB complex. The experiment was replicated at least three times. **g**, ATP inhibits the catalytic activity of the PtuA and PtuB complex in a concentration-dependent manner. All the assays were replicated at least three times. **h**, Effects of UTP, CTP, GTP, dATP, dTTP, dCTP and dGTP on the catalysis of the PtuA and PtuB complex. All the assays were replicated at least three times. **i**, Effects of GDP, CMP, GMP, dAMP, dCMP, dCTP and dGMP on the catalysis of the PtuA and PtuB complex. All the assays were replicated at least three times.

divalent cation among the tested cations in cells,  $Mg^{2+}$  might be the catalytic metal ion used by PtuAB complex under physiological conditions.

To reveal the roles of nucleoside triphosphates (NTPs) in regulating the PtuAB complex, we performed the plasmid nicking assay in the presence of different NTPs. In our plasmid nicking assay, we found that the PtuAB complex can digest plasmids in a concentration-dependent manner (Fig. 6e). Moreover, we noticed that freshly purified PtuAB complex displayed much lower activity than the PtuAB complex stored at 4 °C for a week (Fig. 6f), indicating that ATP molecule may inhibit the nuclease activity of the PtuAB complex. Indeed, further experiments showed that ATP can inhibit the nuclease activity of the PtuAB complex while ADP and AMP do not (Fig. 6f). Subsequent analysis showed that ATP inhibits the activity of PtuAB in a concentration-dependent manner and can completely abolish the activity of PtuAB at concentrations higher than 1 mM (Fig. 6f). We also evaluated the roles of other NTP, deoxy-ribonucleoside triphosphate (dNTP), nucleoside diphosphate (NDP), deoxy-ribonucleoside diphosphate (dNDP), nucleoside monophosphate (NMP), and deoxy-ribonucleoside monophosphate (dNMP) molecules in modulating the activity of PtuAB complex. Unexpectedly, we found that all the NTPs and dNTPs, but not other nucleotides, can suppress the nuclease activity of PtuAB (Fig. 6h,i). Given the

physiological concentration of ATP is over 3 mM in *E. coli*<sup>25</sup>, the nuclease activity of PtuAB is probably inhibited under physiological conditions. When phages infect bacteria, unknown phage factors may activate PtuAB potentially via depleting the ATP bound to PtuA<sup>26</sup>.

### Anti-phage activity of the PtuAB complex

To test the anti-phage activity of PtuAB, we first developed a bacterial colony-forming assay, in which bacteria infected with phages at different multiplicity of infection (MOI) were placed on an agar plate and grown overnight. By comparing the sizes of colonies, we can evaluate the anti-phage effects of PtuAB. We tested the anti-phage activity of PtuAB against phages of T2, T5, T4 and T7 that belong to the Myoviridae, Demereviridae, Myoviridae and Podoviridae families, respectively. Compared to wild-type *E. coli*, *E. coli* expressing PtuAB display effective anti-phage activity against T5 and T7 phages even at a high MOI of 100 (Fig. 7a,b). In contrast, PtuAB provides *E. coli* limited protection against T2 and T4 phages regardless of MOI (Fig. 7c,d). These results suggest that PtuAB restricts phage amplification in a species-dependent manner. Furthermore, *E. coli* with PtuB alone failed to grow well even at low MOIs, suggesting that both PtuA and PtuB are required to confer *E. coli* anti-phage protection (Fig. 7a,b). To determine the growth kinetics of

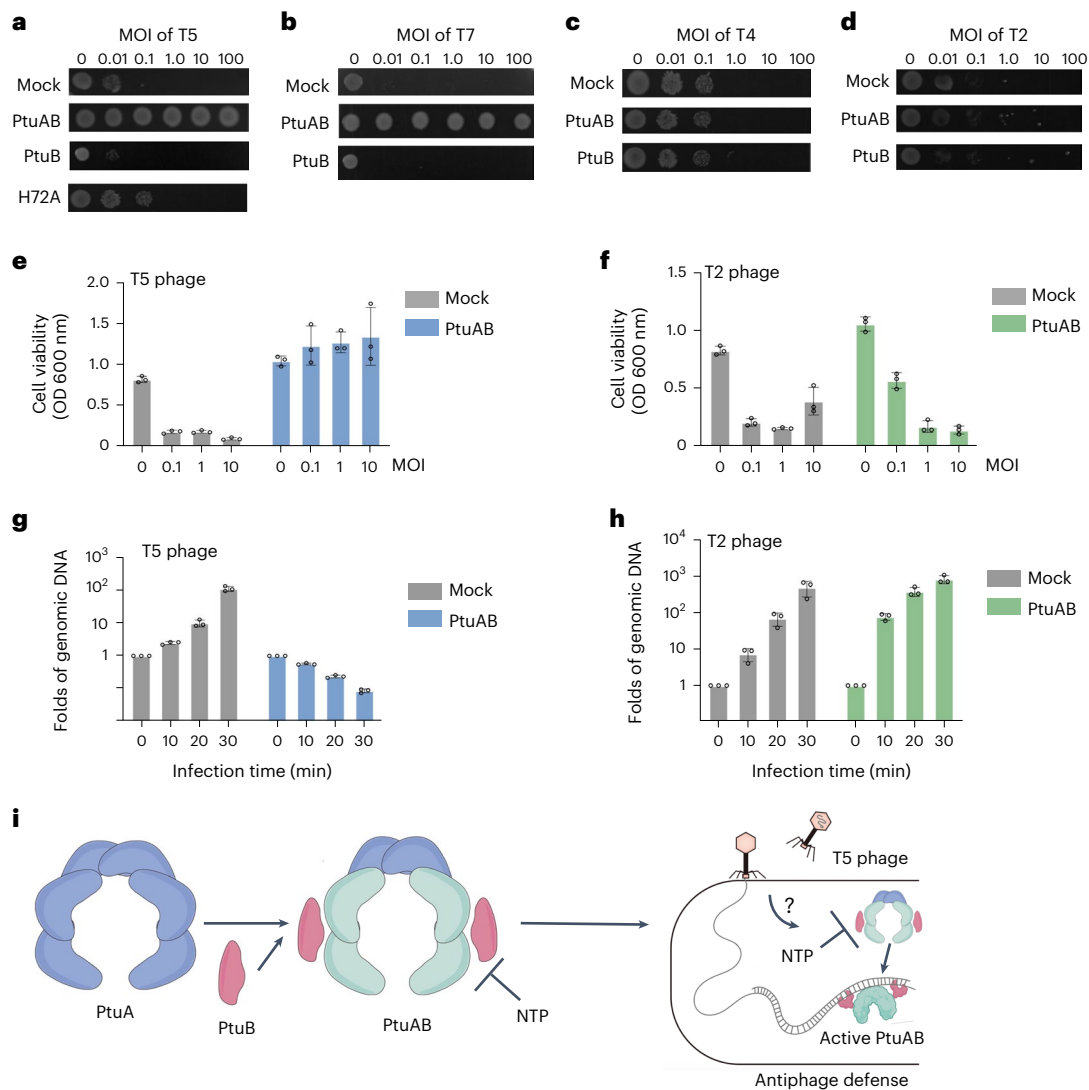


**Fig. 7 | Anti-phage activity of the PtuA and PtuB complex.** **a–d**, Bacteria growth assay showing the effects of PtuAB, PtuB, and PtuB mutant against infections by different phages, including T5 (**a**), T7 (**b**), T4 (**c**) and T2 (**d**). **e, f**, Bacteria survival rates when infected by T5 phage (**e**) and T2 phage (**f**) at different MOI in the presence and absence of the PtuAB system, respectively. Histograms correspond

to the mean of three independent experiments; error bars represent the s.d. **g, h**, Quantified phage genomic DNA at different time points after T5 phage (**g**) and T2 phage (**h**) infection, respectively. Histograms correspond to the mean of three independent experiments; error bars represent the s.d. **i**, Diagram illustrating the assembly and function of the PtuA and PtuB complex.

*E. coli* with or without PtuAB after infection by phages at different MOIs, we made growth curves of *E. coli* after infection. *E. coli* cells without PtuAB displayed growth arrest at low MOIs for both T2 and T5 phages, while *E. coli* with PtuAB resisted T5 infection even at a high MOI but failed to effectively battle with T2 infection at MOIs higher than 0.1 (Fig. 7e, f and Extended Data Fig. 10a, b). Moreover, the growth of *E. coli* with PtuAB is normal in the presence of T5 phage at a high MOI of 2.0 (Extended Data Fig. 10b), suggesting that PtuAB does not confer bacteria anti-phage defense through the abortive infection mechanism.

We further tested whether the nuclease activity of PtuB is required for anti-phage activity. H72A, a catalytic-defective mutant, substantially reduced the anti-phage activity of PtuAB (Fig. 7a and Extended Data Fig. 10c), suggesting that the nuclease activity of PtuB is required for PtuAB anti-phage activity. In addition, the PtuA L81R mutant that disrupted the oligomerization of PtuA and cannot recruit PtuB also failed to confer *E. coli* anti-phage activity (Extended Data Fig. 10d), further supporting that the assembly of PtuAB is critical for its anti-phage activity.

Based on our functional analysis, we postulated that PtuA and PtuB assemble into a complex to restrict phage amplification in bacteria by

selectively degrading the genomic DNA of phages. To test this hypothesis, we decided to quantify the phage genomic DNA in *E. coli* after infection using quantitative polymerase chain reaction (qPCR). After infection, the genomic DNAs of T5 in wild-type *E. coli* increased about ten-fold every 10 min. In contrast, the amplification of T5 genomic DNA was substantially inhibited in *E. coli* expressing PtuAB (Fig. 7g), supporting a mechanism of *E. coli* anti-phage defense mediated by PtuAB via degrading the phage genomic DNA. Consistently, PtuAB, which was shown to have limited anti-phage activity against T2 phages (Fig. 7h), failed to restrict the genomic DNA amplification of T2 phages in cells. Together, these data suggest that PtuAB can confer bacteria immune defense against phage infection by digesting phage genomic DNA in a species-dependent way (Fig. 7i).

## Discussion

In this study, we revealed mechanisms of the assembly and function of Septu, a newly identified anti-phage system in bacteria. The two components of Septu systems, PtuA and PtuB, form a stable complex with a stoichiometry of 6:2, which is critical for the function of the

PtuAB complex. Structural analysis revealed that the oligomerization of PtuA is formed by three pairs of PtuA dimers. Further analysis showed that the unique ATPase domain of PtuA has one  $\beta$ -hairpin and one  $\alpha$ -hairpin compared to other well-studied ATPase domains, which are critical for the unique assembly of PtuA. More strikingly, two pairs of PtuA dimers are responsible for the recruitment of PtuB and resemble each other, but are conformationally different from the third pair, highlighting the different functional roles of PtuA dimers in the complex. Moreover, PtuA has no ATPase activity and may function as an ATP sensor by directly coordinating ATP molecules. Biochemical assays showed that 1 mM ATP but not ADP or AMP can effectively inhibit the nuclease activity of the PtuAB complex. Under physiological conditions, the concentration of ATP in *E. coli* cells is higher than 3.0 mM (ref. 25), which can inhibit the activity of the PtuAB complex. Upon phage infection, potential phage factors may activate PtuAB via depleting the ATP molecules tightly associated with PtuA through an unknown mechanism. It is also possible that phage factors may affect the conformation of the PtuAB complex to activate PtuB. Once activated, the PtuAB complex can selectively cleave the genomic DNA of phages potentially via recognizing unique genome modifications in phages for anti-phage defense<sup>27</sup>.

The mechanism of PtuAB assembly and activation is reminiscent of the nucleotide-binding domain and leucine-rich repeat (NLR) containing a caspase activating and recruitment domain (CARD) 4 (NLRC4) inflammasome, in which the sensor protein NAIPs and the adaptor protein NLRC4 share a similar domain arrangement and form a ring-like oligomer via ATPase domains upon activation<sup>28–30</sup>. Upon activation, the oligomeric NLRC4 inflammasome can activate downstream effector caspase-1 (refs. 31–33). The PtuAB and NLRC4 inflammasome share at least three common features. First, in both systems, the upstream ATPase domain-containing proteins function as sensors and/or adaptors to recruit and facilitate the activation of downstream effector proteins. Second, in both systems, the ATPase domain-containing proteins assemble into large oligomers for function. Third, both systems function as immune surveillance systems to protect hosts from infection by pathogens.

Despite their similarities, PtuAB also displays some unique features from NLRC4 inflammasome. First, the ATPase domain of PtuA is quite unique and has some inserted motifs, which form the structural basis for PtuA to assemble into a unique horseshoe-like structure, contrasting the ring-like structure of NLRC4 inflammasome. Second, PtuA functions as both a sensor and an adaptor, while the NLRC4 inflammasome has NAIP proteins as sensors and NLRC4 proteins as adaptors. Third, the PtuA protomers in the hexamer display different conformations, while all the NLRC4 protomers resemble each other. Fourth, PtuA exists as a constitutive oligomer, while NLRC4 oligomerization is induced. Fifth, the effector protein of PtuAB is a nuclease, while the effector protein in NLRC4 inflammasome is a protease. Lastly, PtuB needs to form a constitutive complex with PtuA for function. Upon activation by NLRC4 inflammasome, caspase-1 will be released from the assembled inflammasome super-complex. Together, these data indicate that PtuA and PtuB assemble into an inflammasome-like complex with unique features for anti-phage activity. Primary sequence analysis showed that many other bacterial immune systems also contain components with ATPase domains and nucleases. As such, it is highly possible that oligomerization mediated by ATPase-domain-containing proteins for anti-phage defense may be universally shared by other ATPase-domain-containing systems in bacteria.

## Online content

Any methods, additional references, Nature Portfolio reporting summaries, source data, extended data, supplementary information, acknowledgements, peer review information; details of author contributions and competing interests; and statements of data and code availability are available at <https://doi.org/10.1038/s41594-023-01172-8>.

## References

- Bernheim, A. & Sorek, R. The pan-immune system of bacteria: antiviral defence as a community resource. *Nat. Rev. Microbiol.* **18**, 113–119 (2020).
- Koonin, E. V., Makarova, K. S. & Wolf, Y. I. Evolutionary genomics of defense systems in Archaea and Bacteria. *Annu Rev. Microbiol.* **71**, 233–261 (2017).
- Dy, R. L., Richter, C., Salmond, G. P. & Fineran, P. C. Remarkable mechanisms in microbes to resist phage infections. *Annu Rev. Virol.* **1**, 307–331 (2014).
- Tock, M. R. & Dryden, D. T. The biology of restriction and anti-restriction. *Curr. Opin. Microbiol.* **8**, 466–472 (2005).
- Barrangou, R. et al. CRISPR provides acquired resistance against viruses in prokaryotes. *Science* **315**, 1709–1712 (2007).
- Makarova, K. S. et al. Evolutionary classification of CRISPR–Cas systems: a burst of class 2 and derived variants. *Nat. Rev. Microbiol.* **18**, 67–83 (2020).
- Swarts, D. C. et al. DNA-guided DNA interference by a prokaryotic Argonaute. *Nature* **507**, 258–261 (2014).
- Swarts, D. C. et al. The evolutionary journey of Argonaute proteins. *Nat. Struct. Mol. Biol.* **21**, 743–753 (2014).
- Duncan-Lowey, B. & Kranzusch, P. J. CBASS phage defense and evolution of antiviral nucleotide signaling. *Curr. Opin. Immunol.* **74**, 156–163 (2022).
- Jinek, M. et al. A programmable dual-RNA-guided DNA endonuclease in adaptive bacterial immunity. *Science* **337**, 816–821 (2012).
- Cong, L. et al. Multiplex genome engineering using CRISPR/Cas systems. *Science* **339**, 819–823 (2013).
- Hsu, P. D., Lander, E. S. & Zhang, F. Development and applications of CRISPR–Cas9 for genome engineering. *Cell* **157**, 1262–1278 (2014).
- Cai, X., Chiu, Y. H. & Chen, Z. J. The cGAS–cGAMP–STING pathway of cytosolic DNA sensing and signaling. *Mol. Cell* **54**, 289–296 (2014).
- Zhang, X., Bai, X. C. & Chen, Z. J. Structures and mechanisms in the cGAS–STING innate immunity pathway. *Immunity* **53**, 43–53 (2020).
- Lowey, B. et al. CBASS immunity uses CARF-related effectors to sense 3′–5′- and 2′–5′-linked cyclic oligonucleotide signals and protect bacteria from phage infection. *Cell* **182**, 38–49 e17 (2020).
- Millman, A., Melamed, S., Amitai, G. & Sorek, R. Diversity and classification of cyclic-oligonucleotide-based anti-phage signalling systems. *Nat. Microbiol.* **5**, 1608–1615 (2020).
- Tal, N. et al. Cyclic CMP and cyclic UMP mediate bacterial immunity against phages. *Cell* **184**, 5728–5739 e5716 (2021).
- Doron, S. et al. Systematic discovery of antiphage defense systems in the microbial pangenome. *Science* <https://doi.org/10.1126/science.aar4120> (2018).
- Gao, L. et al. Diverse enzymatic activities mediate antiviral immunity in prokaryotes. *Science* **369**, 1077–1084 (2020).
- Jumper, J. et al. Highly accurate protein structure prediction with AlphaFold. *Nature* **596**, 583–589 (2021).
- Yang, W. Nucleases: diversity of structure, function and mechanism. *Q. Rev. Biophys.* **44**, 1–93 (2011).
- Holm, L. Dali server: structural unification of protein families. *Nucleic Acids Res.* <https://doi.org/10.1093/nar/gkac387> (2022).
- Hopfner, K. P. et al. Structural biology of Rad50 ATPase: ATP-driven conformational control in DNA double-strand break repair and the ABC-ATPase superfamily. *Cell* **101**, 789–800 (2000).
- Nishimasu, H. et al. Crystal structure of Cas9 in complex with guide RNA and target DNA. *Cell* **156**, 935–949 (2014).
- Buckstein, M. H., He, J. & Rubin, H. Characterization of nucleotide pools as a function of physiological state in *Escherichia coli*. *J. Bacteriol.* **190**, 718–726 (2008).

26. Stokar-Avihail, A. et al. Discovery of phage determinants that confer sensitivity to bacterial immune systems. *Cell* **186**, 1863–1876 e1816 (2023).
27. Wang, S. et al. Landscape of new nuclease-containing antiphage systems in *Escherichia coli* and the counterdefense roles of bacteriophage T4 genome modification. *J. Virol.* **97**, e00599-23 (2023).
28. Lu, A. & Wu, H. Structural mechanisms of inflammasome assembly. *FEBS J.* **282**, 435–444 (2015).
29. Broz, P. & Dixit, V. M. Inflammasomes: mechanism of assembly, regulation and signalling. *Nat. Rev. Immunol.* **16**, 407–420 (2016).
30. Zhao, Y. & Shao, F. Diverse mechanisms for inflammasome sensing of cytosolic bacteria and bacterial virulence. *Curr. Opin. Microbiol.* **29**, 37–42 (2016).
31. Zhang, L. et al. Cryo-EM structure of the activated NAIP2–NLRC4 inflammasome reveals nucleated polymerization. *Science* **350**, 404–409 (2015).
32. Hu, Z. et al. Structural and biochemical basis for induced self-propagation of NLRC4. *Science* **350**, 399–404 (2015).
33. Li, Y. et al. Cryo-EM structures of ASC and NLRC4 CARD filaments reveal a unified mechanism of nucleation and activation of caspase-1. *Proc. Natl Acad. Sci. USA* **115**, 10845–10852 (2018).

**Publisher's note** Springer Nature remains neutral with regard to jurisdictional claims in published maps and institutional affiliations.

Springer Nature or its licensor (e.g. a society or other partner) holds exclusive rights to this article under a publishing agreement with the author(s) or other rightsholder(s); author self-archiving of the accepted manuscript version of this article is solely governed by the terms of such publishing agreement and applicable law.

© The Author(s), under exclusive licence to Springer Nature America, Inc. 2024

## Methods

### Bacterial strains and phages

*E. coli* strain ATCC25922, BL21 (DE3) and DH5 $\alpha$  were cultured routinely in LB at 37 °C. Phages T2, T4, T5 and T7 were obtained from DSMZ and propagated in *E. coli* BL21 (DE3).

### Phylogenetic tree construction

CD-HIT (version 4.8.1) was utilized to perform efficient clustering of all amino acid sequences in this study<sup>34</sup>. The sequence identity threshold was set to 0.75 to ensure reliable clustering results. Additionally, a word length of 5 was chosen for the analysis, allowing for a balance between accuracy and computational efficiency. Following the clustering process, representative sequences were extracted based on the clustering results. These representative sequences were then subjected to sequence alignment using MAFFT v7.475 in auto mode<sup>35</sup>. To improve alignment quality, the aligned sequences were further trimmed using trimal v1.4 in automated1 mode<sup>36</sup>.

For phylogenetic tree construction, the maximum likelihood (ML) method was employed using Iqtree v1.6.5 (ref. 37). The ML tree was built with 1,000 ultrafast bootstrap replicates and 1,000 Shimodaira-Hasegawa-like approximate likelihood ratio tests, ensuring robustness and reliability of the tree topology. Finally, the constructed ML tree was visualized using iTOL<sup>38</sup>, an online tool specifically designed for the display, annotation and management of phylogenetic and other types of trees.

### Protein expression and purification

Genes encoding PtuA and PtuB were amplified from *E. coli* strain ATCC 25922 genomic DNA and cloned into a vector derived from pET-28a (+) (Novagen), containing a C-terminal His<sub>6</sub> tag (Table 1). Proteins were overexpressed in *E. coli* BL21 (DE3) at 18 °C for 18 h.

For protein purification, cell pellets were resuspended in buffer A (20 mM Tris-HCl, 150 mM NaCl, pH 8.0) followed by cell lysis and centrifugation to remove cell debris. The supernatant was incubated with 1 ml Iminodiacetic-Acid-nickel magnetic beads (BeaverBeads, Beaverbio) pre-equilibrated with buffer A. The beads were washed with buffer A supplemented with 10 mM imidazole to remove nonspecifically bound proteins, and then the target proteins were eluted by buffer A supplemented with 250 mM imidazole. The target proteins were concentrated and further purified by a gel-filtration column (Superdex 200 10/300 GL, GE Healthcare) with SEC buffer (20 mM HEPES and 150 mM NaCl, pH 7.5).

### Cryo-EM data collection

Three microliters PtuA or PtuAB sample at 2.0 mg ml<sup>-1</sup> was applied to a glow-discharged Quantifoil RL2/1.3400 mesh gold grid (Electron Microscopy Sciences) followed by 4 s blotting at 4 °C using an FEI Vitrobot Mark IV. All the grids were screened using a ThermoFisher Glacios microscope (OSU Center for Electron Microscopy and Analysis). We collected all the datasets using a 300 kV Titan Krios microscope (FEI) equipped with a K3 direct electron detector (Gatan) using EPU v2.11.1 at the National Cancer Institute Cryo-Electron Microscopy Center. 7,042 micrographs for the PtuAB complex and 6,992 micrographs for PtuA were collected by a counting mode, with 50 total frames per movie, 50.0 electrons per Å<sup>2</sup> accumulated dose, and a physical pixel size of 1.12 Å, respectively.

### Cryo-EM structure reconstruction

All the collected frames were motion-corrected and dose-weighted in MotionCor2 (ref. 39). Initial contrast transfer function parameters were estimated by CTFFIND4 (ref. 40). All the particles were automatically picked using CryoSPARC v4.0.0 (ref. 41).

For PtuA, 11,005,697 particles were picked for multiple rounds of 2D and 3D classification in CryoSPARC<sup>41</sup>. Eventually, 779,494 particles were selected for the final reconstruction and refinement, leading to a map of 2.9 Å (Extended Data Fig. 3a–c).

For PtuA reconstructed from the PtuAB dataset, initial particle picking resulted in 1,183,080 particles. After 2D and 3D classification within CryoSPARC<sup>41</sup>, 2,379,256 particles were selected for final refinement to generate a map of 2.6 Å (Extended Data Fig. 7b). For the PtuAB complex, a similar procedure was performed as the PtuA except particle picking using a larger box size (Extended Data Fig. 8a). The local resolution for PtuB is very low in the initial reconstructed map. To improve the resolution of PtuB, we generated a mask covering a PtuA side dimer and a PtuB for focused refinement, which significantly improved the local resolution of PtuB. Then, we aligned the focused refined map onto the original map to generate a composite map of PtuAB in Chimera<sup>42</sup>.

All the maps were filtered according to their local resolutions with *b*-factor sharpening within CryoSPARC<sup>41</sup>. Softwares (other than CryoSPARC) for structure determination were supported by SBGrid<sup>43</sup>.

### Cryo-EM model building and refinement

The AlphaFold models for PtuA and PtuB were fitted into cryo-EM maps using Chimera<sup>42</sup>. Manual adjustments were done using Coot<sup>44</sup>, followed by refinement in PHENIX<sup>45</sup>. All the structural representations were generated using ChimeraX<sup>42</sup> or PyMol<sup>46</sup>.

### Native mass spectrometry analysis

The sample underwent online buffer exchange before mass spectrometry analysis. A mobile phase of 200 mM ammonium acetate at pH 7.0 was maintained at a flow rate of 50  $\mu$ l min<sup>-1</sup>. A Vanquish Duo ultra-high-performance liquid chromatography system (Thermo Scientific) equipped with a dual pump and autosampler was used to load protein samples without further purification into a MAbPac size exclusion column (MAbPac SEC1, 2.1  $\times$  300 mm, 300 Å, 5  $\mu$ m; Thermo Scientific, 008789). One microgram of the sample was injected onto the column and was further tracked by ultraviolet absorbance. From 0 min to 16.8 min, the flow was diverted from the column to the mass spectrometer, while after this time (16.8 min to 30 min), flow was diverted to the waste. The timing of this switch was optimized to allow for buffer-exchanged protein samples to make it to the mass spectrometer, while salts from the original buffer were passed to the waste. Buffer exchanged samples were then analyzed using a Q Exactive Ultra-High Mass Range Hybrid Quadrupole-Orbitrap mass spectrometer (Thermo Scientific). The following settings were used for mass spectrometry analysis. Scan range was set to 1,000–20,000. Resolution was set to 12,500. Number of microscans was set to 5. Maximum injection time was set to 200 ms. Sheath gas was set to 60 psi. Auxiliary and sweep gas were set to 0 psi. Spray voltage was set to 3.85 kV in positive ion mode. Capillary temperature was set to 275 °C. S-lens RF level was set to 200 V. In-source trapping was set to -120 V. In-source dissociation was set to 5 V. Source direct current (DC) offset was set to 21 V. Injection flatapole DC was set to 5 V. Inter flatapole lens was set to 4 V. Bent flatapole DC was set to 2 V. Tapping gas pressure was set to 7. The total run time for the method was 30 min. The mass spectrum was deconvolved using Unidec<sup>47</sup>.

### Mass photometry analysis

Refeyn TwoMP mass photometer was used for mass photometry experiments. Glass coverslips (Thorlabs) were cleaned using water, 100% isopropanol, water, 100% isopropanol and water and were dried using nitrogen. Similarly cleaned reusable silicone gaskets with culture wells (Sigma) were affixed to the glass coverslips. Mass measurements were done in either 50 mM Tris (pH 8.0), 150 mM NaCl, and 0.5 mM tris(2-carboxyethyl)phosphine (TCEP) or 200 mM ammonium acetate. First, calibrations were obtained using an equimolar mixture of beta-amylase (monomer 56 kDa, dimer 112 kDa, tetramer 224 kDa) and thyroglobulin (monomer 330 kDa, dimer 660 kDa) in each buffer. Sample stocks were added to wells containing buffer to

achieve nanomolar concentrations required for mass photometry. Data acquisition was done using AcquireMP and data analysis was done using DiscoverMP. Three measurements were done in each buffer. Masses were calculated by applying appropriate calibration. In both buffers, the sample showed presence of monomer and dimer. Due to high buffer background seen in 50 mM Tris (pH 8.0), 150 mM NaCl and 0.5 mM TCEP, measurements were also conducted in 200 mM ammonium acetate. The masses obtained in each buffer are as follows. In 50 mM Tris (pH 8.0), 150 mM NaCl and 0.5 mM TCEP: monomer  $49.0 \pm 0$  kDa (from two measurements as monomer was not visible in one of the three measurements), dimer  $107.7 \pm 2.1$  kDa. In 200 mM ammonium acetate: monomer  $54.7 \pm 1.5$  kDa, dimer  $108.7 \pm 0.6$  kDa.

### Plasmid nicking assay

Plasmid nicking assay was carried out in a 10- $\mu$ l reaction system containing 200 ng pUC19 plasmid, 50 nM PtuaB proteins, 1 mM MnCl<sub>2</sub> and 20 mM Tris-HCl (pH 8.0). The reactions were performed at 37 °C for 15 min and terminated by adding 10 mM ethylenediaminetetraacetic acid. The samples were analyzed using 1% agarose gels.

### ATPase assay

The ATPase activity was measured using a phosphate detection kit (Solarbio, BC0965) that monitored the amount of free phosphate released according to the manufacturer's protocol. The reactions were performed with various concentrations of PtuaA or PtuaB (50 nM and 1  $\mu$ M), with or without 20 ng  $\mu$ l<sup>-1</sup> pUC19, by a microplate reader (CLARIO star plus) at 660 nm.

### Phage titer determination

Phage titer was determined using the small drop plaque assay as described previously<sup>48</sup>. Briefly, *E. coli* BL21(DE3) were mixed with MMB agar (LB supplemented with 5 mM MgCl<sub>2</sub>, 0.1 mM MnCl<sub>2</sub>, 5 mM CaCl<sub>2</sub> and 0.6% agar), and serial ten-fold dilutions of phages were added on top of them for overnight incubation at 37 °C. Phage titer was determined by calculating plaque-forming units (PFUs) per milliliter. Three technical replicates were conducted for each phage.

### Bacterial colony-forming assay

*E. coli* cells with or without the Septu defense system grew at 37 °C and were induced by 0.1 mM isopropyl  $\beta$ -D-1-thiogalactopyranoside at OD<sub>600</sub> of 0.2. *E. coli* cells were infected by phages at MOIs of 100, 10, 1, 0.1, 0.01 or 0 and spotted on 1.5% agar plates for overnight culture at 37 °C. The mock data were generated using bacteria with a pET28a vector.

### Bacterial growth assay

Bacteria with or without the Septu defense system were cultured at 37 °C to OD<sub>600</sub> of 0.2. Then, 180  $\mu$ l cultured bacteria were transferred into a 96-well plate, followed by adding 20  $\mu$ l phages at MOIs of 2, 0.02 or 0. The OD<sub>600</sub> of the bacteria was monitored using a microplate reader (CLARIO star plus) every 5 min for a total duration of 6 h.

### Phage genomic DNA quantification assay

Bacteria with or without the Septu system were infected by T2 or T5 phages with an MOI of 1. Cells were collected at 0, 10, 20 or 30 min after infection, and their total DNA was extracted using TIANGEN Bacteria DNA Kit (TIANGEN, 4992448). We used 20 ng DNA as templates, 2  $\mu$ M of phage-specific primers or host-specific primers, and 2 $\times$  ChamQ Universal SYBR qPCR Master Mix (Vazyme, Q711-02/03) for each PCR reaction. A CFX Connect Real-Time System (Bio-Rad) was used to amplify the DNA templates. Phage DNA copy number was normalized. DNA copy number at 0 min was set to 1, relative to which the DNA copy numbers at other time points were quantified as described previously<sup>49</sup>. All the experiments have three replicates.

### Reporting summary

Further information on research design is available in the Nature Portfolio Reporting Summary linked to this article.

### Data availability

Accession numbers for PtuaA and PtuaB are as follows: (coordinates of atomic models: 8SUX, 8EE4, 8EE7 and 8EEA, deposited to Protein Data Bank), and (density map: EMD-40779, EMD-28045, EMD-28048 and EMD-28049, deposited to Electron Microscopy Data Bank). All data needed to evaluate the conclusions are present in the paper.

### References

- Li, W. & Godzik, A. Cd-hit: a fast program for clustering and comparing large sets of protein or nucleotide sequences. *Bioinformatics* **22**, 1658–1659 (2006).
- Katoh, K. & Standley, D. M. MAFFT multiple sequence alignment software version 7: improvements in performance and usability. *Mol. Biol. Evol.* **30**, 772–780 (2013).
- Capella-Gutierrez, S., Silla-Martinez, J. M. & Gabaldon, T. trimAL: a tool for automated alignment trimming in large-scale phylogenetic analyses. *Bioinformatics* **25**, 1972–1973 (2009).
- Hoang, D. T., Chernomor, O., von Haeseler, A., Minh, B. Q. & Vinh, L. S. UFBoot2: improving the ultrafast bootstrap approximation. *Mol. Biol. Evol.* **35**, 518–522 (2018).
- Letunic, I. & Bork, P. Interactive Tree Of Life (iTOL) v5: an online tool for phylogenetic tree display and annotation. *Nucleic Acids Res.* **49**, W293–W296 (2021).
- Zheng, S. Q. et al. MotionCor2: anisotropic correction of beam-induced motion for improved cryo-electron microscopy. *Nat. Methods* <https://doi.org/10.1038/nmeth.4193> (2017).
- Rohou, A. & Grigorieff, N. CTFIND4: fast and accurate defocus estimation from electron micrographs. *J. Struct. Biol.* **192**, 216–221 (2015).
- Punjani, A., Rubinstein, J. L., Fleet, D. J. & Brubaker, M. A. cryoSPARC: algorithms for rapid unsupervised cryo-EM structure determination. *Nat. Methods* **14**, 290–296 (2017).
- Pettersen, E. F. et al. UCSF Chimera—a visualization system for exploratory research and analysis. *J. Comput. Chem.* **25**, 1605–1612 (2004).
- Morin, A. et al. Collaboration gets the most out of software. *eLife* **2**, e01456 (2013).
- Emsley, P. & Cowtan, K. Coot: model-building tools for molecular graphics. *Acta Crystallogr. D* **60**, 2126–2132 (2004).
- Adams, P. D. et al. PHENIX: a comprehensive Python-based system for macromolecular structure solution. *Acta Crystallogr. D* **66**, 213–221 (2010).
- Delano, W. L. *The PyMol Molecular Graphics System* (PyMol, 2002).
- Marty, M. T. et al. Bayesian deconvolution of mass and ion mobility spectra: from binary interactions to polydisperse ensembles. *Anal. Chem.* **87**, 4370–4376 (2015).
- Mazzocco, A., Waddell, T. E., Lingohr, E. & Johnson, R. P. Enumeration of bacteriophages using the small drop plaque assay system. *Methods Mol. Biol.* **501**, 81–85 (2009).
- Chou-Zheng, L. & Hatoum-Aslan, A. A type III-A CRISPR-Cas system employs degradosome nucleases to ensure robust immunity. *eLife* <https://doi.org/10.7554/eLife.45393> (2019).

### Acknowledgements

Grid screening was performed at OSU CEMAS with the assistance of G. Grandinetti and Y. Narui. Cryo-EM data were collected with the assistance of A. D. Wier, T. J. Edwards, T. Fox and J. Wang at the National Cancer Institute Cryo-Electron Microscopy Center supported by grants from the NIH National Institute of General Medical Sciences

(GM103310). A. Rish was supported by an NIH T32 (GM118291-05 and GM144293-01). The funders had no role in study design, data collection and analysis, decision to publish or preparation of the manuscript. Source data are provided with this paper.

### Author contributions

Q.C., Y.Y. and T.-M.F. conceived the project. Y.L., Z.S., X.-Y.Y., M.Z. and J.X. performed molecular cloning and biochemical purification of the PtuA, PtuB, PtuAB and all the mutants. Y.L. and M.Z. performed the ATPase assay, plasmids nicking assays, bacterial growth assay and phage genomic DNA quantification assay. Z.S. and T.-M.F. prepared grids, determined the cryo-EM structures and built the models. S.P.C., J.G. and M.K. performed the native mass spectrometry analysis and I.A.M. did the mass photometry analysis under the supervision of V.H.W. T.-M.F., Y.Y., Q.C., A.D.R. and C.C. analyzed the data. T.-M.F. wrote the manuscript with inputs from all the authors.

### Competing interests

All authors declare they have no competing interests.

### Additional information

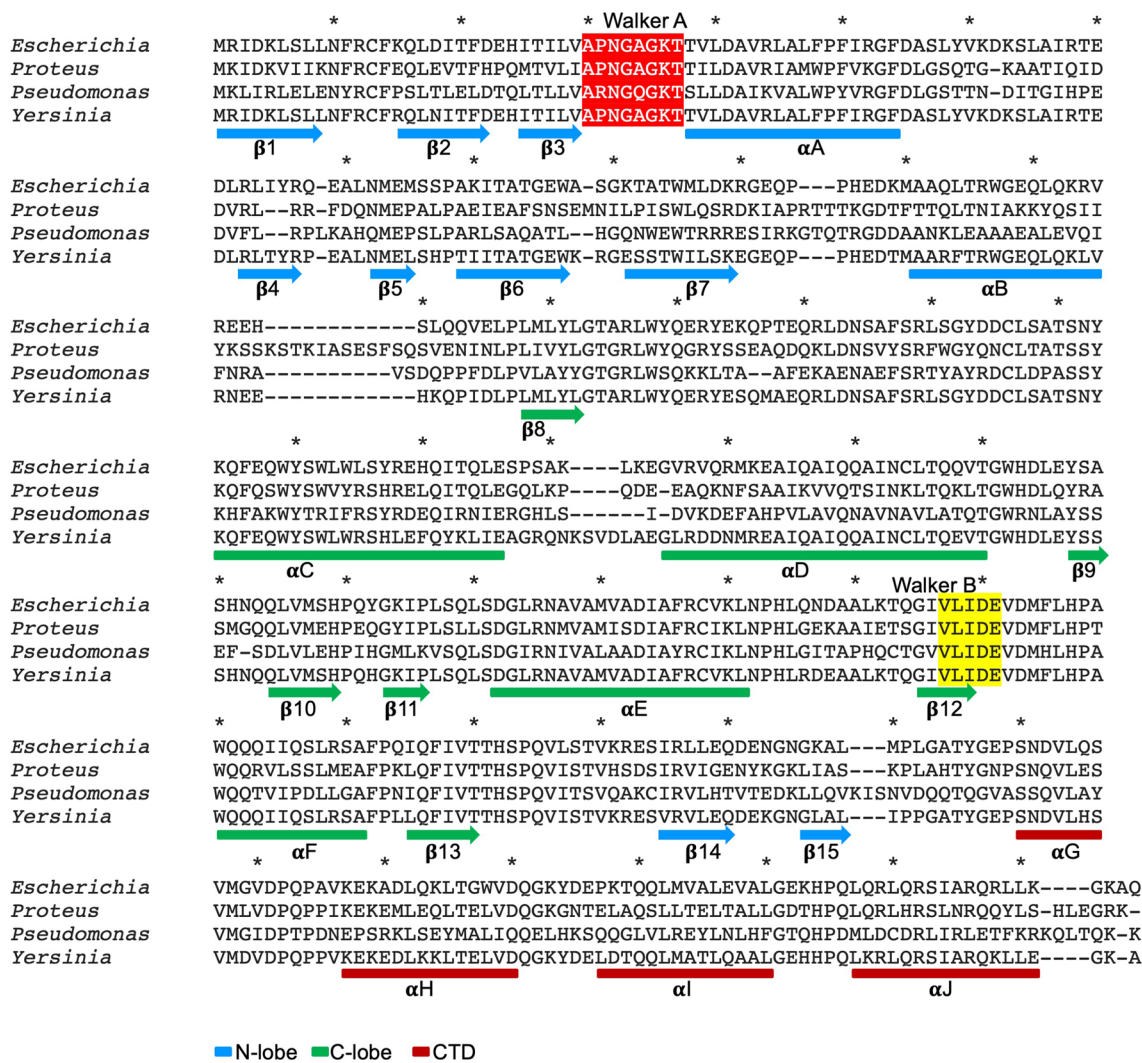
**Extended data** is available for this paper at <https://doi.org/10.1038/s41594-023-01172-8>.

**Supplementary information** The online version contains supplementary material available at <https://doi.org/10.1038/s41594-023-01172-8>.

**Correspondence and requests for materials** should be addressed to Qiang Chen, Tian-Min Fu or Yamei Yu.

**Peer review information** *Nature Structural & Molecular Biology* thanks Jun-Jie Liu, Qian Yin and the other, anonymous, reviewer(s) for their contribution to the peer review of this work. Sara Osman was the primary editor on this article and managed its editorial process and peer review in collaboration with the rest of the editorial team. Peer reviewer reports are available.

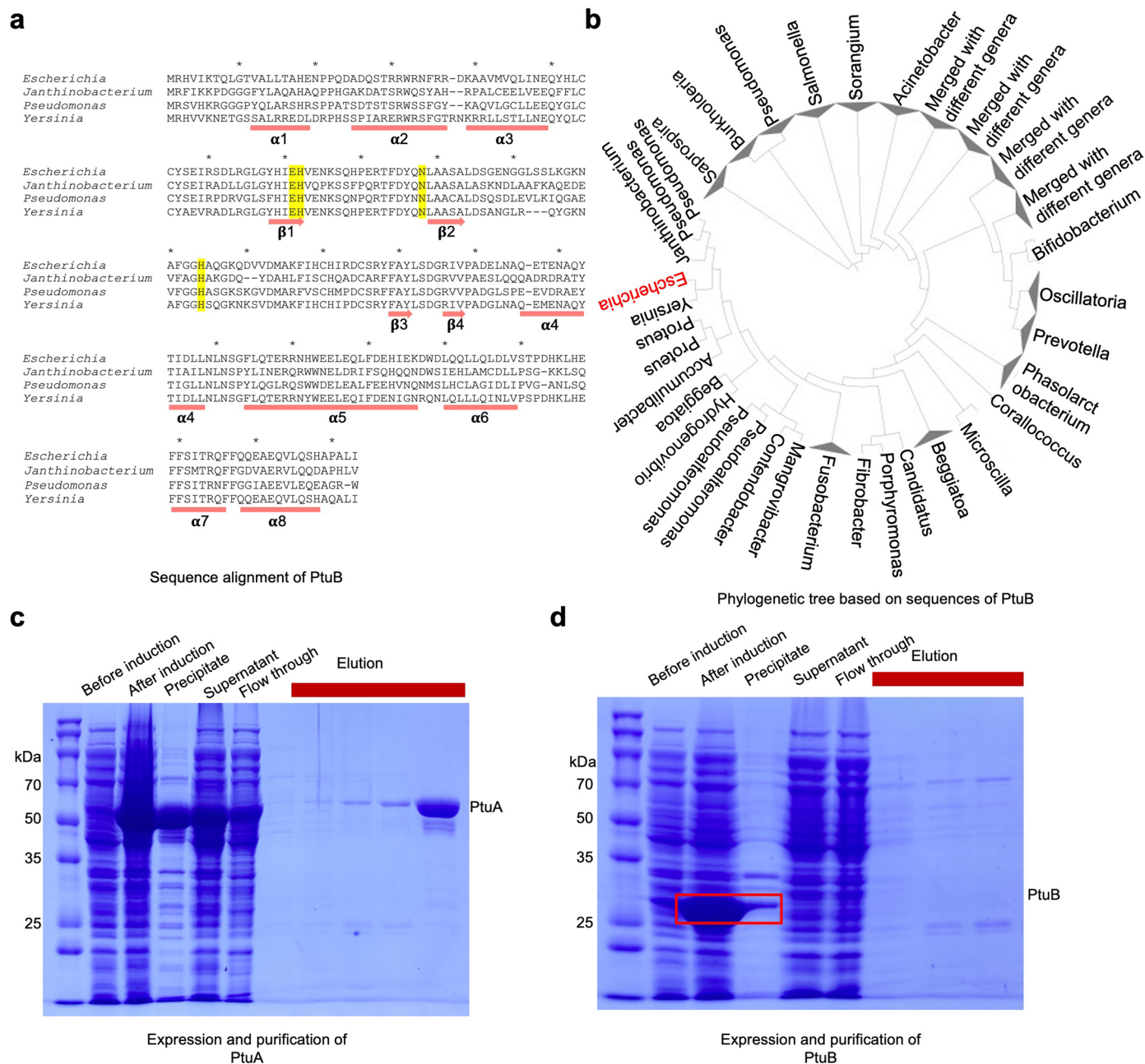
**Reprints and permissions information** is available at [www.nature.com/reprints](http://www.nature.com/reprints).



## Sequence alignment of Ptua

**Extended Data Fig. 1 | Sequence Alignment of Ptua from Different Species.** Sequence alignment of Ptua from *Escherichia coli* (Genbank ID AIL15948.1), *Proteus mirabilis* (Genbank ID AGS60026.1), *Pseudomonas veronii* (Genbank ID KRP82805.1), and *Yersinia enterocolitica* (Genbank ID AHM71342.1) with

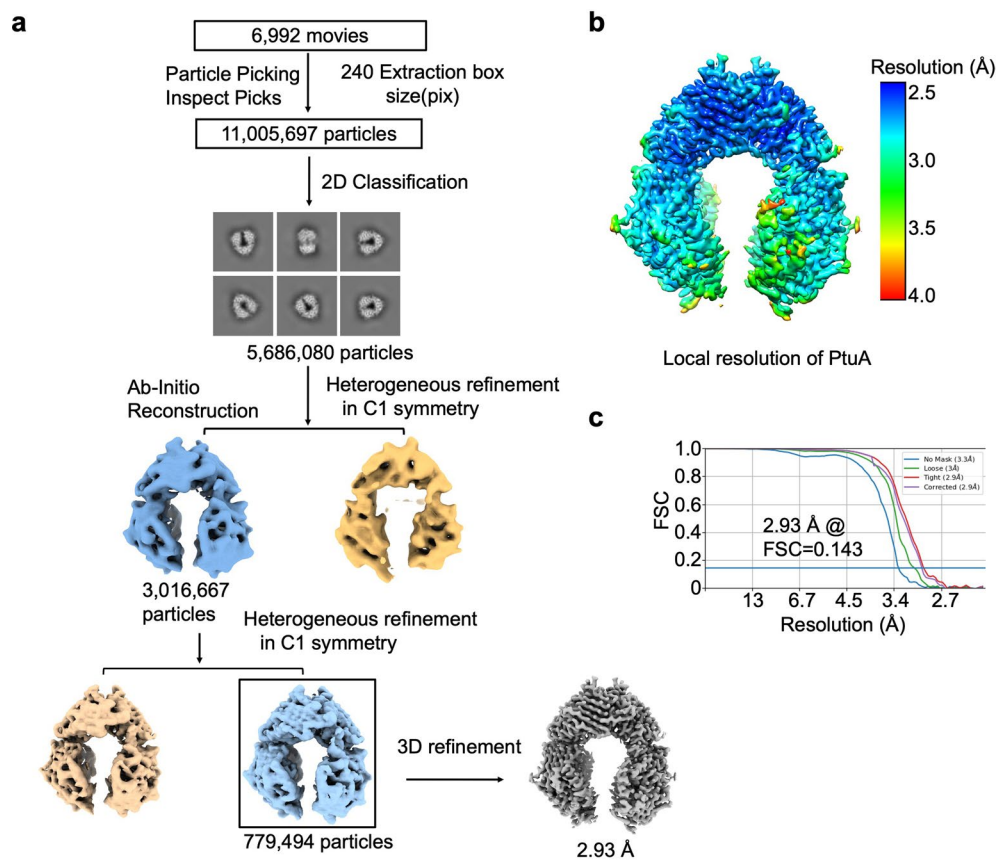
secondary structural elements labeled below. NTD was highlighted in blue, and CTD was highlighted in green. Walker A motif, Walker B motif, and a signature motif critical for coordinating ATP were highlighted in red, yellow, and green, respectively.



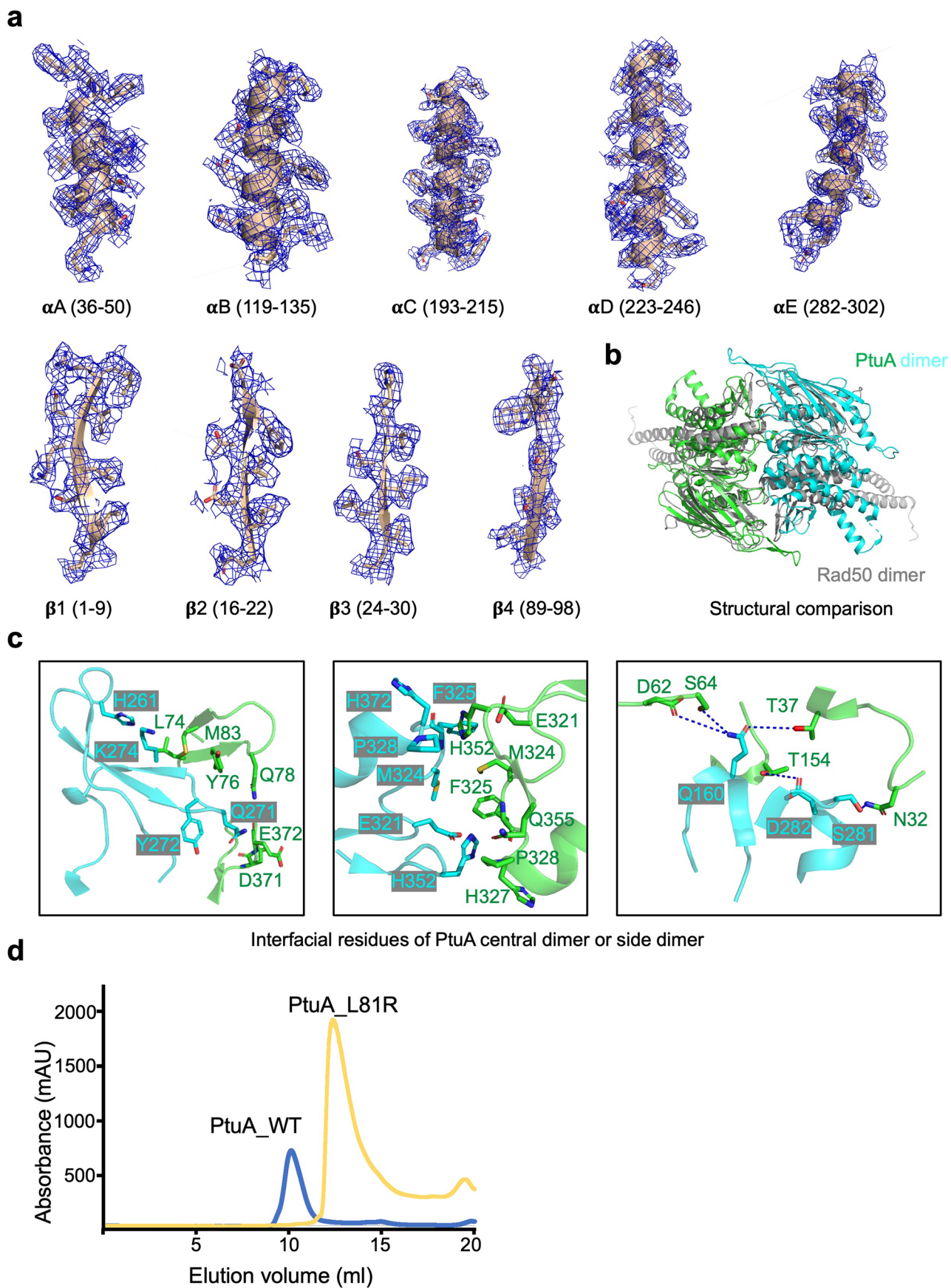
### Extended Data Fig. 2 | Analysis and Purification of Ptua and Ptub.

**a**, Sequence alignment of Ptub from *Escherichia coli* (Genbank ID AIL15172.1), *Janthinobacterium agaricidammosum* (Genbank ID CDG84671.1), *Yersinia enterocolitica* (Genbank ID AHM71343.2), and *Pseudomonas veronii* (Genbank ID KRP82804.1) with secondary structural elements labelled below. Catalytic residues of Ptub were highlighted in yellow. **b**, Diagram of phylogenetic trees

of Ptub from different species. **c**, SDS-PAGE analysis of Ptua expression and purification via Ni<sup>2+</sup> affinity column. The experiment was replicated at least three times. **d**, SDS-PAGE analysis of Ptub expression and purification via Ni<sup>2+</sup> affinity column. Bands of Ptub were highlighted in a red box. The experiment was replicated at least three times.

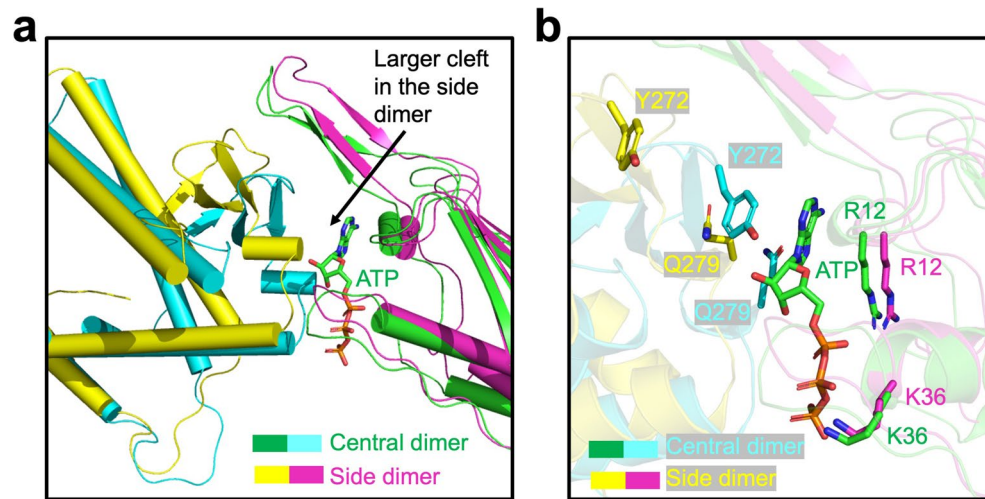


**Extended Data Fig. 3 | Structure Determination of Ptua.** **a**, Workflow of Ptua 3D reconstruction using CryoSPARC. **b**, Local resolutions of the reconstructions of Ptua. Resolutions are color-coded by scale bars. **c**, Fourier shell correlation (FSC) curve of 3D reconstructed Ptua.

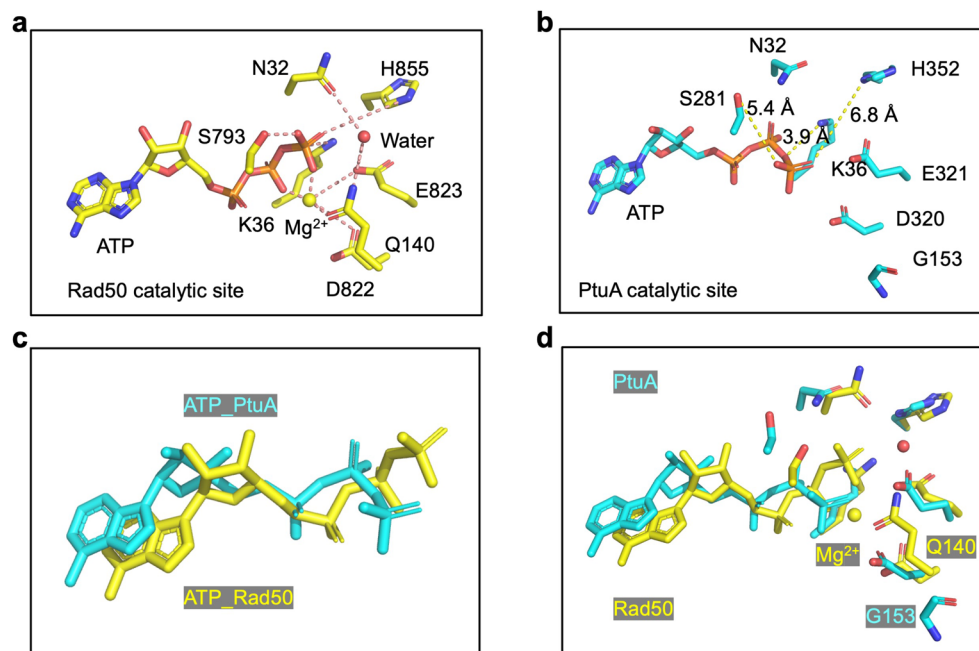


**Extended Data Fig. 4 | Cryo-EM Density of Ptua and Structure comparison.**  
**a**, Representative segments of Ptua cryo-EM density map with the final atomic model (2.0  $\sigma$ ). **b**, Overlaid structures of Ptua (green and cyan) and Rad50 dimers

(Grey). **c**, Residues on the dimeric interface of Ptua were highlighted in sticks. **d**, Gel filtration profiles of Ptua wild type (blue) and L81R mutant (gold), showing that L81R disrupted the Ptua hexamer.

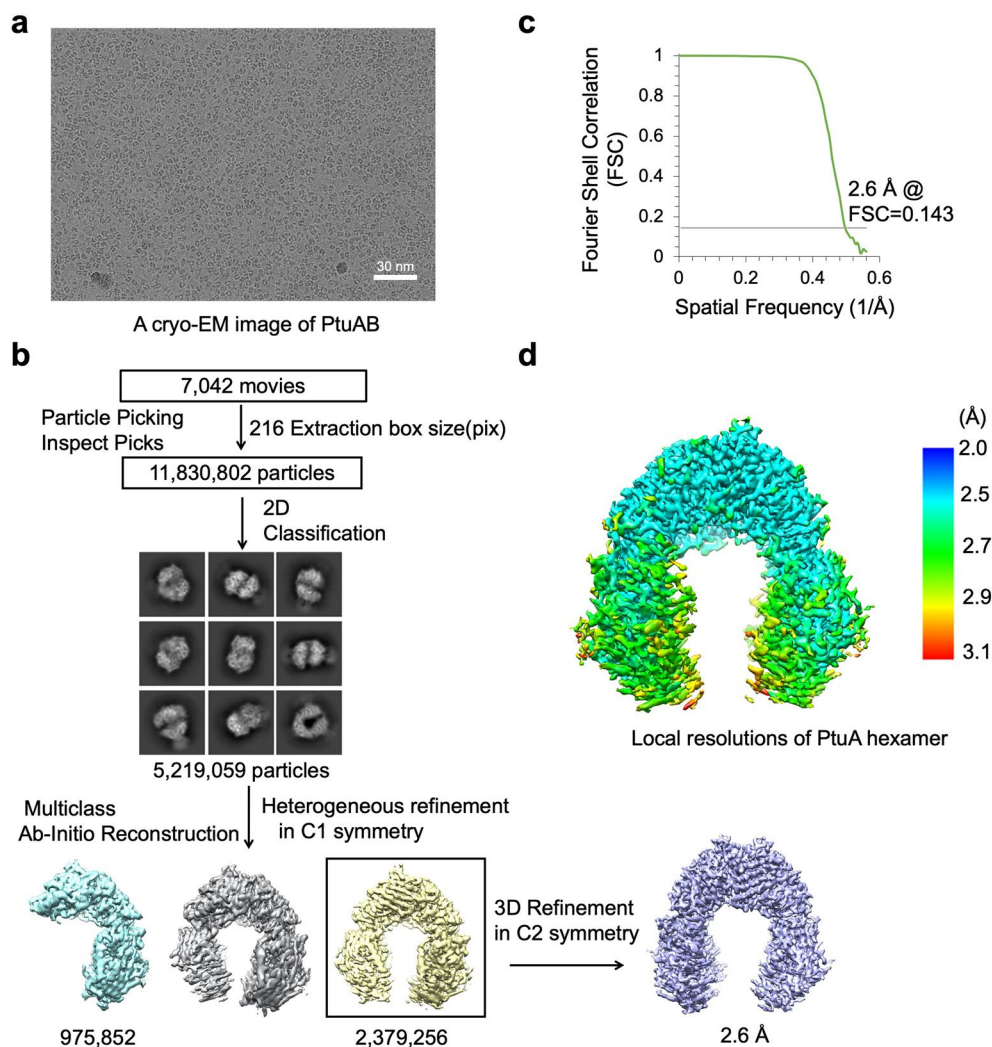


**Extended Data Fig. 5 | Comparison of ATP Binding Sites.** **a**, Overlaid structures of the central dimer (cyan and green) and the side dimer (yellow and magenta), revealing a larger cleft at the ATP binding site of the side dimer. ATP is highlighted as sticks. **b**, Key residues for ATP coordination are highlighted as sticks. Key residues are far away from the potential ATP binding site in the side dimer.



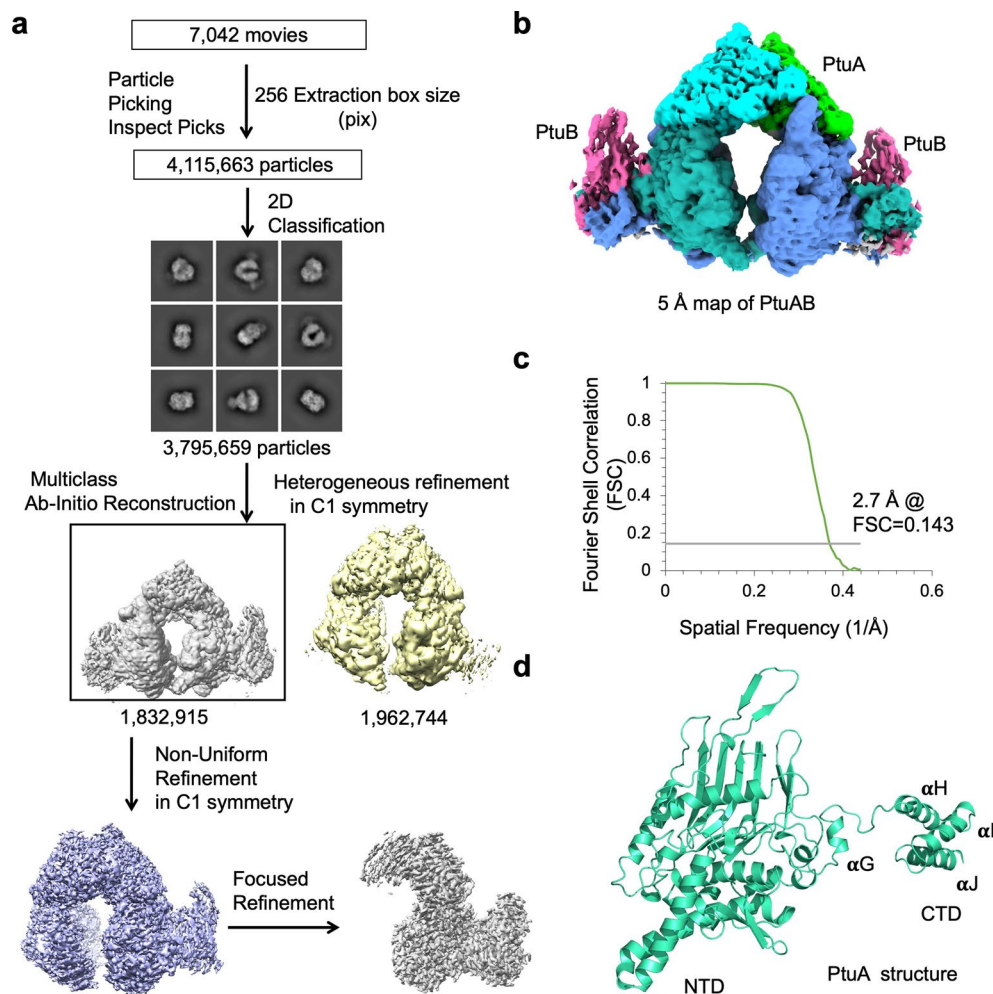
**Extended Data Fig. 6 | ATP Catalysis. a**, ATP catalytic site of Rad50, highlighting an extensive hydrogen bond network formed by key residues and magnesium (sphere). **b**, ATP catalytic site of PtuA. Key residues are not well aligned to form

hydrogen bonds with ATP. **c**, Comparison of ATP molecules in PtuA (cyan) and Rad50 (yellow), revealing the unique configuration of ATP in PtuA. **d**, Overlaid structures of ATP catalytic sites in PtuA (cyan) and Rad50 (yellow).



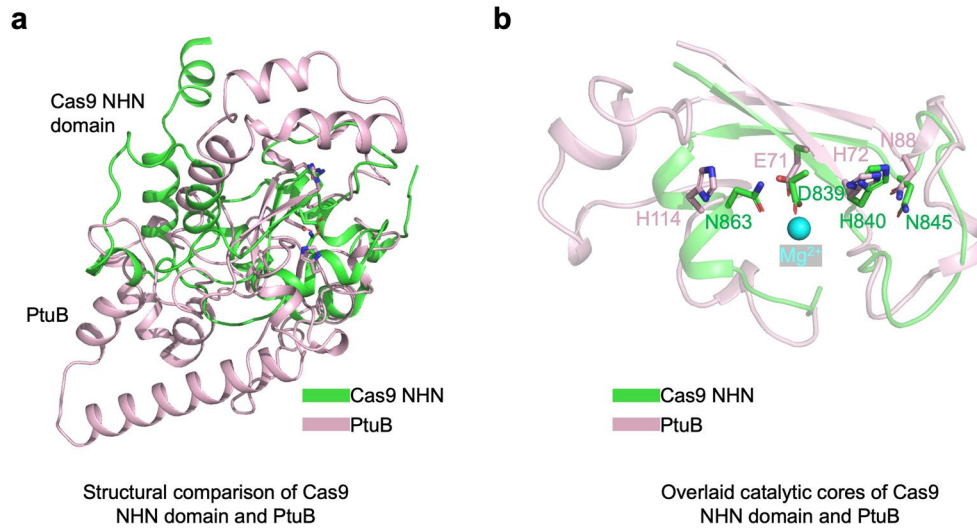
**Extended Data Fig. 7 | Structural Reconstruction of PtuaA from the PtuaAB Dataset.** **a**, A representative cryo-EM image of the PtuaA and PtuaB complex. Thousands of images were collected. **b**, Workflow of PtuaA 3D reconstruction

using CryoSPARC. **c**, Fourier shell correlation (FSC) curve of 3D reconstructed PtuaA. **d**, Local resolutions of the reconstructions of PtuaA. Resolutions are color-coded by scale bars.

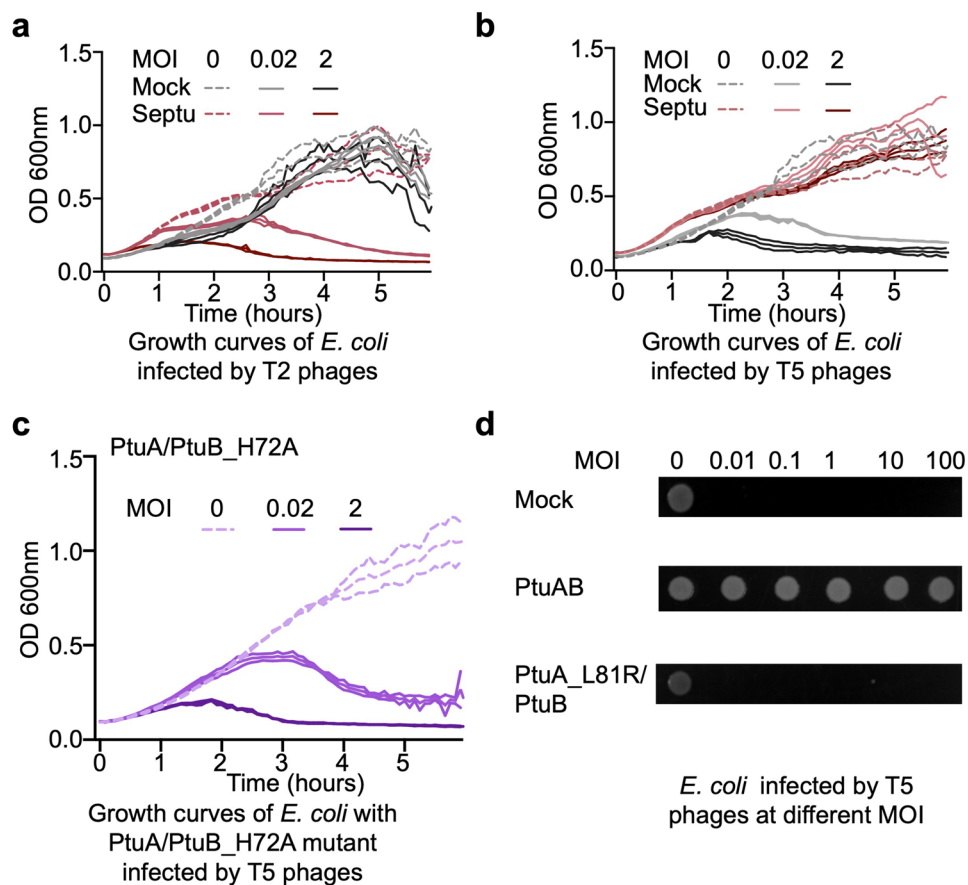


**Extended Data Fig. 8 | Cryo-EM Structure Reconstruction of the PtuA and PtuB complex.** **a**, Workflow of the PtuAB complex 3D structure reconstruction using CryoSPARC. **b**, Initial cryo-EM map of the PtuAB complex at a resolution

of 5 Å. **c**, FSC curve of the focused refined cryo-EM map of the PtuAB complex. **d**, Ribbon diagram of the full-length PtuA, revealing that PtuA CTD is composed of three  $\alpha$ -helices.



**Extended Data Fig. 9 | Structural Comparison of PtuB and Cas9.** **a**, Overlaid structures of PtuB (pink) and the NHN domain of Cas9 (green) revealing their similarity. **b**, Overlaid catalytic cores of PtuB (pink) and the NHN domain of Cas9 (green) with catalytic residues highlighted in sticks.



**Extended Data Fig. 10 | Anti-phage Immune Defense by the PtuA and PtuB Complex.** **a**, Bacteria growth curves with T2 phage infection at different MOI. **b**, Bacteria growth curves with T5 phage infection at different MOI. **c**, PtuA/PtuB\_H72A failed to confer anti-phage protection as evaluated by bacterial growth

assay. The experiment was replicated more than three times. **d**, PtuA L81R/PtuB failed to confer anti-phage protection as evaluated by bacterial colony-forming assay. The experiment was replicated more than three times.

## Reporting Summary

Nature Portfolio wishes to improve the reproducibility of the work that we publish. This form provides structure for consistency and transparency in reporting. For further information on Nature Portfolio policies, see our [Editorial Policies](#) and the [Editorial Policy Checklist](#).

### Statistics

For all statistical analyses, confirm that the following items are present in the figure legend, table legend, main text, or Methods section.

- | n/a                                 | Confirmed  |
|-------------------------------------|--|
| <input type="checkbox"/>            | <input checked="" type="checkbox"/> The exact sample size ( $n$ ) for each experimental group/condition, given as a discrete number and unit of measurement  |
| <input type="checkbox"/>            | <input checked="" type="checkbox"/> A statement on whether measurements were taken from distinct samples or whether the same sample was measured repeatedly  |
| <input checked="" type="checkbox"/> | <input type="checkbox"/> The statistical test(s) used AND whether they are one- or two-sided<br><i>Only common tests should be described solely by name; describe more complex techniques in the Methods section.</i>  |
| <input type="checkbox"/>            | <input checked="" type="checkbox"/> A description of all covariates tested   |
| <input type="checkbox"/>            | <input checked="" type="checkbox"/> A description of any assumptions or corrections, such as tests of normality and adjustment for multiple comparisons  |
| <input type="checkbox"/>            | <input checked="" type="checkbox"/> A full description of the statistical parameters including central tendency (e.g. means) or other basic estimates (e.g. regression coefficient) AND variation (e.g. standard deviation) or associated estimates of uncertainty (e.g. confidence intervals) |
| <input checked="" type="checkbox"/> | <input type="checkbox"/> For null hypothesis testing, the test statistic (e.g. $F$ , $t$ , $r$ ) with confidence intervals, effect sizes, degrees of freedom and $P$ value noted<br><i>Give <math>P</math> values as exact values whenever suitable.</i>                                       |
| <input checked="" type="checkbox"/> | <input type="checkbox"/> For Bayesian analysis, information on the choice of priors and Markov chain Monte Carlo settings  |
| <input checked="" type="checkbox"/> | <input type="checkbox"/> For hierarchical and complex designs, identification of the appropriate level for tests and full reporting of outcomes  |
| <input checked="" type="checkbox"/> | <input type="checkbox"/> Estimates of effect sizes (e.g. Cohen's $d$ , Pearson's $r$ ), indicating how they were calculated  |

*Our web collection on [statistics for biologists](#) contains articles on many of the points above.*

### Software and code

Policy information about [availability of computer code](#)

Data collection

Data analysis

For manuscripts utilizing custom algorithms or software that are central to the research but not yet described in published literature, software must be made available to editors and reviewers. We strongly encourage code deposition in a community repository (e.g. GitHub). See the Nature Portfolio [guidelines for submitting code & software](#) for further information.

### Data

Policy information about [availability of data](#)

All manuscripts must include a [data availability statement](#). This statement should provide the following information, where applicable:

- Accession codes, unique identifiers, or web links for publicly available datasets
- A description of any restrictions on data availability
- For clinical datasets or third party data, please ensure that the statement adheres to our [policy](#)

Accession numbers for Ptua and PtuaB are as follows: (coordinates of atomic models: 8SUX, 8EE4, 8EE7, and 8EEA, deposited to Protein Data Bank), and (density map: EMD-40779, EMD-28045, EMD-28048, and EMD-28049, deposited to Electron Microscopy Data Bank). All other data needed to evaluate the conclusions are presented in the paper.

## Research involving human participants, their data, or biological material

Policy information about studies with [human participants or human data](#). See also policy information about [sex, gender \(identity/presentation\), and sexual orientation](#) and [race, ethnicity and racism](#).

Reporting on sex and gender	N/A
Reporting on race, ethnicity, or other socially relevant groupings	N/A
Population characteristics	N/A
Recruitment	N/A
Ethics oversight	N/A

Note that full information on the approval of the study protocol must also be provided in the manuscript.

## Field-specific reporting

Please select the one below that is the best fit for your research. If you are not sure, read the appropriate sections before making your selection.

Life sciences       Behavioural & social sciences       Ecological, evolutionary & environmental sciences

For a reference copy of the document with all sections, see [nature.com/documents/nr-reporting-summary-flat.pdf](https://www.nature.com/documents/nr-reporting-summary-flat.pdf)

## Life sciences study design

All studies must disclose on these points even when the disclosure is negative.

Sample size	No any sample sizes or statistical analyses were pre-determined. In the cryo-EM datasets, final images numbers for each datasets were collected to obtain sufficient EM maps that allowed for unambiguous atomic model building, which suggested sufficient sample size. For biochemical experiments, no information was derived about a population based on sampling.
Data exclusions	In cryo-EM data processing, bad images with CTF outliers (ice contamination or crushed) were removed form further analysis. We also discarded "junk" particles that could not be classified into useful 3D refinemet during 2D or 3D classifications. Those procedures are widely used practice in the cryo-EM field. No other data were excluded from analysis.
Replication	All biochemical experiments were performed independently at least three times with similar results.
Randomization	For cryo-EM maps determination, FSCs were calculated using two independent havles of the datasets, into which the particles were randomly allocated. Randomization is not relevant to other in vitro biochemical analysis.
Blinding	Blinding was unnecessary for cryo-EM analysis and biochemical assays.

## Reporting for specific materials, systems and methods

We require information from authors about some types of materials, experimental systems and methods used in many studies. Here, indicate whether each material, system or method listed is relevant to your study. If you are not sure if a list item applies to your research, read the appropriate section before selecting a response.

### Materials & experimental systems

n/a	Involvement in the study
<input checked="" type="checkbox"/>	<input type="checkbox"/> Antibodies
<input checked="" type="checkbox"/>	<input type="checkbox"/> Eukaryotic cell lines
<input checked="" type="checkbox"/>	<input type="checkbox"/> Palaeontology and archaeology
<input checked="" type="checkbox"/>	<input type="checkbox"/> Animals and other organisms
<input checked="" type="checkbox"/>	<input type="checkbox"/> Clinical data
<input checked="" type="checkbox"/>	<input type="checkbox"/> Dual use research of concern
<input checked="" type="checkbox"/>	<input type="checkbox"/> Plants

### Methods

n/a	Involvement in the study
<input checked="" type="checkbox"/>	<input type="checkbox"/> ChIP-seq
<input checked="" type="checkbox"/>	<input type="checkbox"/> Flow cytometry
<input checked="" type="checkbox"/>	<input type="checkbox"/> MRI-based neuroimaging